Title
Ultra Large Field-of-view Fluorescent Biomedical Scanner Imaging System

Author
Ling, Yuye

Publication Date
2013

Peer reviewed|Thesis/dissertation

University of California
Los Angeles

Ultra Large Field-of-view Fluorescent Biomedical Scanner Imaging System

A thesis submitted in partial satisfaction
of the requirements for the degree
Master of Science in Electrical Engineering

by

Yuye Ling

2013

Abstract of the Thesis

Ultra Large Field-of-view Fluorescent Biomedical Scanner Imaging System

by

Yuye Ling

Master of Science in Electrical Engineering

University of California, Los Angeles, 2013

Professor Aydogan Ozcan, Chair

In this project, we proposed and built a dual-mode biomedical imaging modality, which based on a very cost-effective flatbed scanner. The modifications of the scanner was mainly made in three aspects, system control, illumination, and post-processing procedure. First of all, we rewrote the scanner driver based on the open-sourced SANE backend to gain the complete control over the scanner and to accommodate our special necessities, such as altering motor step and sample rate. Then, an attachment, which provided the external illumination for dark field and fluorescent, was designed and printed (by 3D printer). Finally, after getting the raw images of the sample, several extra post-processing procedures were taken to further improve both the image quality and the user experience. In this dissertation, we will explain the aforementioned modifications that we have made in details. We will also present and discuss the experimental results of our system. Currently, the proposed system is able to detect 10 μm fluorescent beads in fluorescent mode and 4 μm non-fluorescent beads in dark-field over an entire area as large as 20.4 cm $\times$ 17.8 cm. The system shows great potential some specific biomedical imaging problems that require huge throughput, such as detecting circulating tumor cells.

The thesis of Yuye Ling is approved.

Eric P.-Y. Chiou

Oscar Stafsudd

Aydogan Ozcan, Committee Chair

University of California, Los Angeles

2013

Table of Contents

List of Figures

List of Tables

CHAPTER 1

Introduction

Since its first introduction to biology community by Antoni van Leeuwenhoek in the late 17^{th} century, the optical microscope has been playing a vital role in human's exploration of nature and science in various disciplines such as physics, physiology, medicine and many others. Regardless of its simplicity (Figure 1.1), the optical microscope has contributed to numerous exciting discoveries and breakthroughs. Even in the current century, most medical laboratories still rely heavily on this "ancient" technology for daily inspections. Compared with other higher-resolution image modalities such as transmission electron microscopy (TEM) and scanning electron microscopy (SEM), optical microscopy has several advantages especially in biological settings:

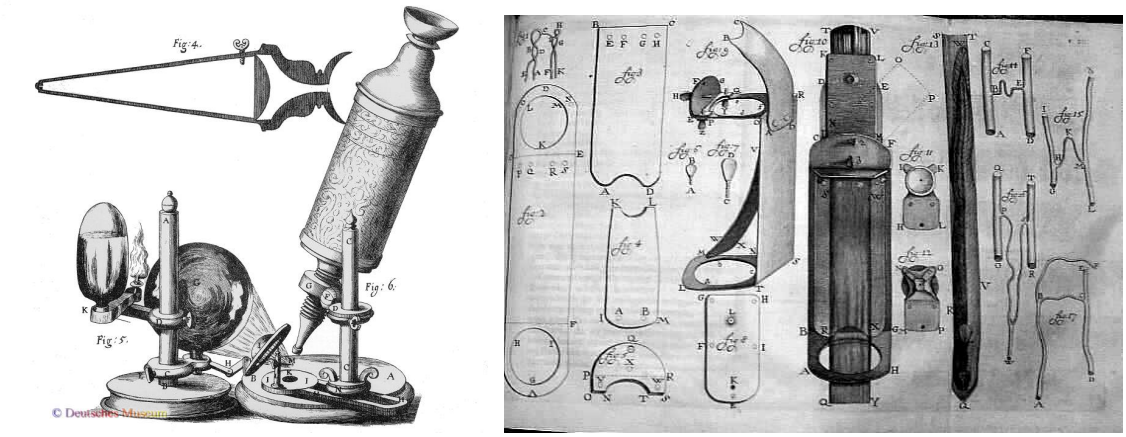

(a) (b)

Figure 1.1: (a) A microscope of Robert Hooke [Hoo67] (b) Drawing of microscopes owned by Antonie van Leeuwenhoek [Bak56]

- **Simple and less destructive sample preparation:** In most cases, optical microscopy requires much less sample treatment than other imaging techniques. There is no special treatment needed for optical microscopy. On the other hand, the TEM can only image electronic transparent samples, while the SEM requires a conductive surface over the sample, which is usually fulfilled by depositing metals films before inspection. Since most biological samples will not survive either the electron bombards or vacuum deposition, both TEM and SEM seem impractical for live sample observation.

- **Versatile contrast method:** Optical microscopy offers various contrast enhancement methods including bright-field, dark-field, phase-contrast, differential interference contrast, and fluorescent microscopy [Lac99]. Among these techniques, fluorescent microscopy is the most widely used one in biological applications due to its capability of visualizing a specific type of molecules based on selective excitation of fluorophore-labeled cells. Thus, this technique is unique in optical microscopy and especially advantageous when we want to study the intracellular distribution, dynamics, and statistics of certain molecules among large volume of other molecules [Lac99].

- **Balanced field of view:** The field-of-view of an optical microscope is dependant on the magnification of the objective lens. It generally ranges from hundreds of microns to several millimeters. This makes optical microscope a better candidate to certain biomedical applications that require high throughput, such as flow cytometry. On the other hand, the field of view of the TEM and SEM is usually much smaller.

- **High speed acquisition:** In both TEM and SEM system, specialized electron detectors and scanning mechanism are used to detect the object, which is very time consuming even for a tiny area. On the other hand, optical mi-

croscope uses image sensors such as charge-coupled device (CCD) and complementary metal-oxide-semiconductor (CMOS), which can easily achieve video rate recording and greatly facilitate the imaging of live cells.

- **Relatively low cost:** Compared with TEM or SEM system, conventional optical microscope requires much less complex component and is thus cheaper.

Because the fluorescent microscopy is a major, if not the most frequently employed, contrast method in biological settings, I will discuss this in details in the following section.

1.1 Fluorescence microscope

The invention of the fluorescence microscope can be dated back to the early 20^{th} century, when scientists were attempting to use ultraviolet light source to achieve higher resolution. However, it did not become popular until a method of localizing antigen was proposed by Coon and Kaplan in 1950 [CK50]. In their study, the antibodies were labelled with fluorescent dyes to facilitate the antibody-antigen interactions. Before this attempt, the fluorescent microscopy was only applicable to intrinsically fluorescent samples, which contain tryptophan, tyrosine, or phenylalanine.

However, in most cases, the extra labelling process using antibodies-fluorescent label pair is prone to bringing unnecessary disturbance to the sample. Therefore, biologists are more interested in finding a non-disturbing approach. There comes the fluorescent protein expression techniques. In 1961, Shimomura first purified green fluorescent protein (GFP) from *Aequorea victoria* [Shi05] shown in Figure 1.2. The chemical structure and genetic sequence of GFP was later reported by Shimomura in 1979 [Shi79] and Prasher in 1992 [PEW92], respectively. Finally,

in 1994, Chalfie et al. managed to express natural fluorescent proteins in living organisms [CTE94]. These joint efforts led to Martin Chalfie, Osamu Shimomura and Roger Y. Tsien's sharing of the 2008 Nobel Prize in Chemistry for their discovery and development of the GFP [Nob08].

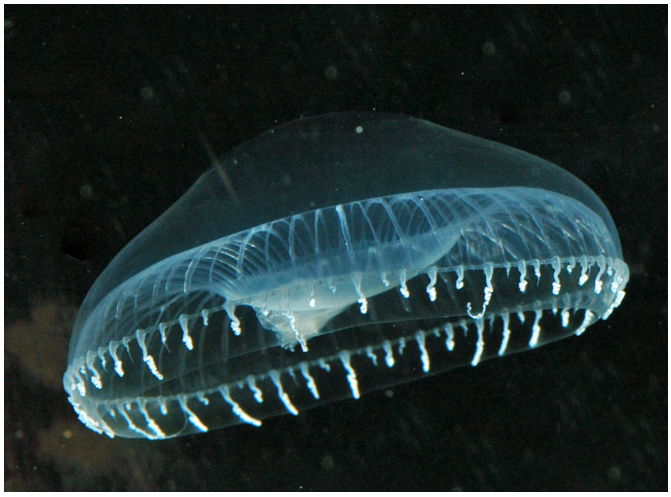

Figure 1.2: *Aequorea victoria*. Courtesy of Sierra Blakely

1.1.1 Principle

Fluorescence is a physical process, in which a fluorescent molecule is first excited by a higher frequency incident photon, and later re-emits a photon at lower frequency. The process can be described by the following two equations:

$$S_0 + h\nu_{\text{excitation}} \rightarrow S_1 \tag{1.1}$$

$$S_1 \rightarrow S_0 + h\nu_{\text{emission}} + \text{dissipation} \tag{1.2}$$

Equation 1.1 describes the "photon absorption" of the molecule, where S_0 stands for the ground state of the substance, h represents the Planck's constant, $\nu_{\text{excitation}}$ is the frequency of the incident photon, and S_1 stands for the excitation state of the substance. Equation 1.2 describes the "photon emission" that happens

afterwards, where ν_{emission} is the frequency of the photon that is re-emitted by the substance, which is usually referred to as the "fluorescent light". In most cases, the wavelength of the re-emitted light is longer than that of the absorbed light because that part of the energy is dissipated through heat transferring during the process. The process can also be illustrated by Figure 1.3.

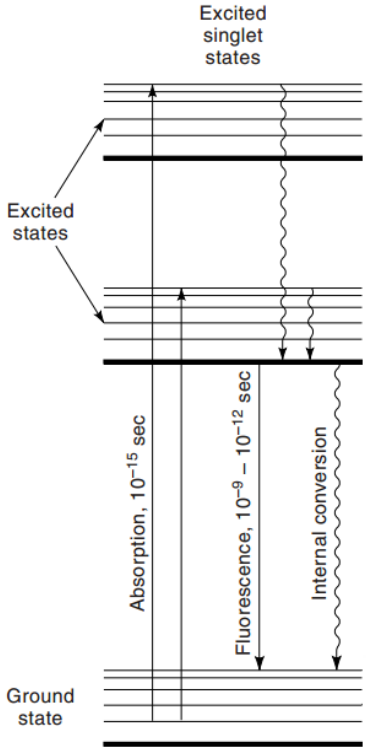

Figure 1.3: The Jablonski diagram of absorbance, non-radiative decay, and fluorescence. [Lac99]

1.1.2 Configuration and working principle

Figure 1.5(a) shows a typical configuration of a conventional fluorescence microscope. The system includes an epi-illuminator, a dichroic mirror, an emission filter, an excitation filter, objective lens and eye piece. Among those components, the filter sets (dichroic mirror, emission filter, and excitation filter) are the most

essential ones. The dichroic mirror is usually a multi-layer dielectric band-stop interferometer, and it reflects the excitation light and transmits the emission light when mounted at 45°. The transmission spectrum of the filters is depicted in Figure 1.4.

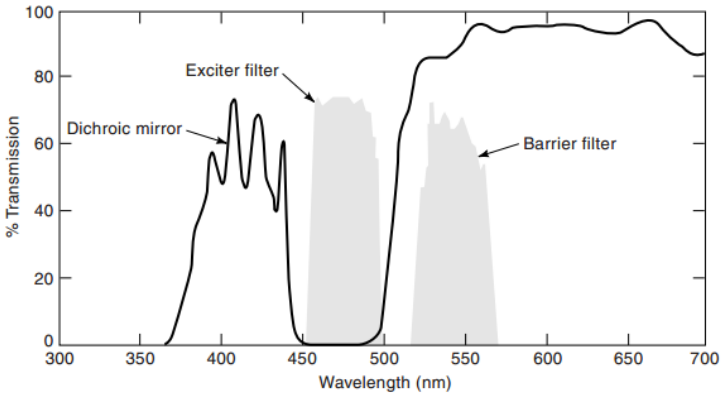

Figure 1.4: The transmission spectrum of dichroic mirror, emission filter (barrier filter), and excitation filter (exciter filter). [Lac99]

When the fluorescence microscope is working, the spectrum of the illumination from the epi-illuminator is first narrowed by the excitation filter. The dichroic filter then reflects the illumination beam to the specimen and later transmits the re-emitted fluorescent light from the specimen to the emission filter and the detector.

In order to achieve satisfactory fluorescent images, the filter sets are designed so that the pass band of the excitation filter matches the trough of the dichroic mirror, while the pass band of the emission filter matches that of the dichroic mirror. Moreover, a high-NA objective lens is also preferred, especially for imaging dim fluorescent specimens. Thus, we will be able to get a clean fluorescent image of the specimen without the irrelevant background. Figure 1.6 shows two fluorescent images of a multiple labeled sample taken in FITC (green) channel and TRITC (red) channel, respectively.

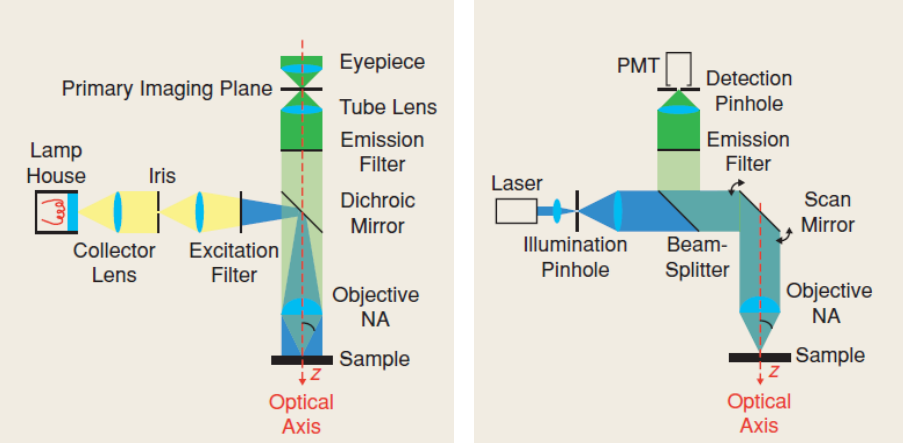

(a) (b)

Figure 1.5: Schematic drawing of (a) conventional fluorescence microscope (b) confocal microscope [VAV06]

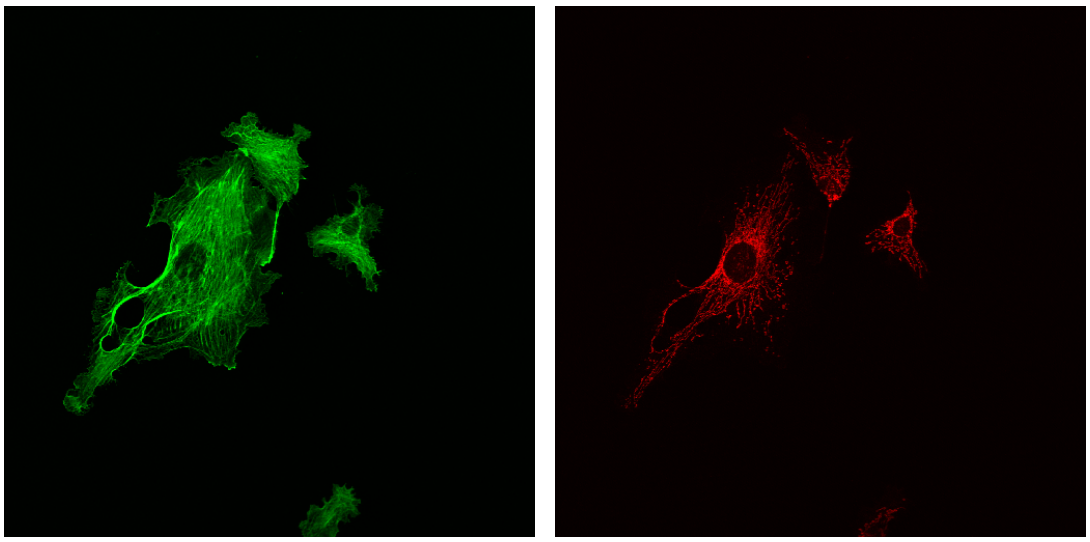

(a) (b)

Figure 1.6: Fluorescent images of a multiple labeled sample taken in (a) FITC (green) channel and (b) TRITC (red) channel

1.2 Confocal laser scanning microscope

For conventional fluorescent microscopy, the images taken from thick samples such as tissues sections usually suffer from lower resolution and reduced contrast, because the emitted fluorescent signals from not only the focal plane but also the adjacent planes will be allowed to the detector. This issue is stressed in confocal laser scanning microscopy by using a focused laser beam to excite the sample and inserting a pinhole in the imaging plane in front of the detector as shown in 1.5(b). More importantly, these modifications also provide the new technique with the ability of optical sectioning, one specific layer of the object is imaged at a time, and further the three-dimensional reconstruction of the entire thick specimen. Before we start to depict the working principles of the confocal laser scanning microscope, we will first discuss several most commonly used criteria that defines the performance of the microscope system.

- *Numerical Aperture (NA)* defines the maximum angle of the diffracted light from the sample that can be finally collected by the objective lens and is defined by:

$$\mathrm{NA} = n \sin\theta \tag{1.3}$$

  where n is the refractive index of the medium surrounding the objective, and θ gives the half of the acceptance angle of the lens.

- *Lateral Resolution* describes the ability of an optical system to distinguish two closely placed objects such as bars or points. More quantitatively, the pattern is said to be resolved if the central diffraction spot of one object coincides with the first diffraction minimum of the other according to the Rayleigh Criterion. The resolution power of a microscope system can generally be predicted according to the following equation,

$$d = \frac{0.61\lambda}{\mathrm{NA}} \tag{1.4}$$

where d is the minimum resolvable distance and λ is the wavelength of the probing light. Therefore, the theoretical limit, which is usually known as diffraction limit, of a conventional microscope operating at 546 nm (green light) is about 0.26 μm when the NA is equal to 1.

- *Depth Of Field* defines the thickness Z of the object along the z axis that is in focus:

$$Z = \frac{n\lambda}{\mathrm{NA}^2} \tag{1.5}$$

where n is the refractive index of the surrounding medium.

- *Field of View* describes the area one can see through the microscope system. It is usually measured by the field-of-view number or simply the field number. The diameter of the scene (in μm) you can see is given by:

$$\text{Field size} = \frac{\text{Field number}}{\text{Objective Magnification}} \tag{1.6}$$

For most conventional microscopes, the field number of the eyepieces is around 22. Then, based on the objective magnification, the actual field size can range from several hundreds of nanometers to several microns. In scenarios other than microscopy, the field of view is also defined by the area instead of the diameter.

- *Space Bandwidth Product (SBP)* SBP is usually taken to measure the amount of the information within an optical image, and defined by [GL67],

$$\mathrm{SBP} = \frac{\mathrm{A}}{\mathrm{R}^2} \tag{1.7}$$

where A is the size of the image and R is its resolution.

Now, let's turn to the optical configuration of the confocal laser scanning microscope. A laser beam is first expanded by a lens to fill the aperture of the objective so that the focused beam will form a tiny spot to excite the specimen.

Then, only the fluorophore within that tiny spot will emit fluorescent light. The fluorescent light will be transmitted through the dichroic mirror as well as the emission filter. However, unlike the conventional fluorescent microscope, a pinhole situates in front of the detector. The pinhole is optically confocal with the illumination spot that is in the object plane, hence the pinhole will reject most fluorescent signals coming from the planes other than the object plane (Figure 1.7).

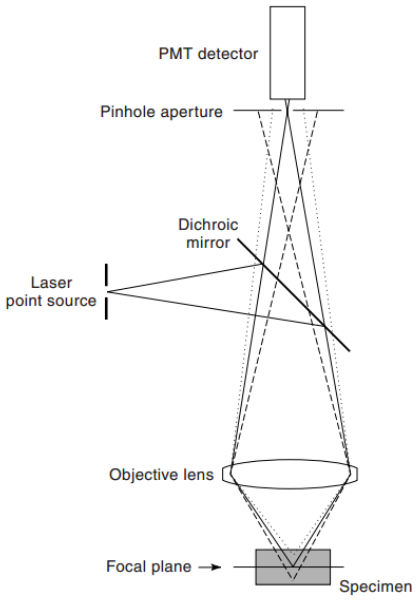

Figure 1.7: The confocal principle in epi-fluorescent laser scanning microscopy [MD12]

In comparison with the conventional fluorescent microscope, the confocal laser scanning microscope offers several advantages including improved lateral resolution, controllable axis resolution, and enhanced image contrast. For example, the lateral resolution of confocal microscope can exceed that of the conventional fluorescent microscope by a factor of $\sim$1.4 [Paw95].

The key feature that makes confocal microscopy unique is its optical sectioning ability. Thanks to the pinhole placed right in the conjugate plane to the object plane, only the most in-focus fluorescent emission will be collected by the detector, which is placed behind the pinhole. Most out-of-focus secondary fluorescent emission coming from the volume will be exclude. Moreover, if we further take Equation 1.5 into consideration, we can find that the depth of the field is anti-proportional to the NA of the objective, which means the higher the NA of the objective is, the thinner the optical slice will be. With this optical sectioning capability, the confocal microscope can build up an image series along the z direction up to hundreds of microscope at a step size as low as 1 micron (Figure 1.8).

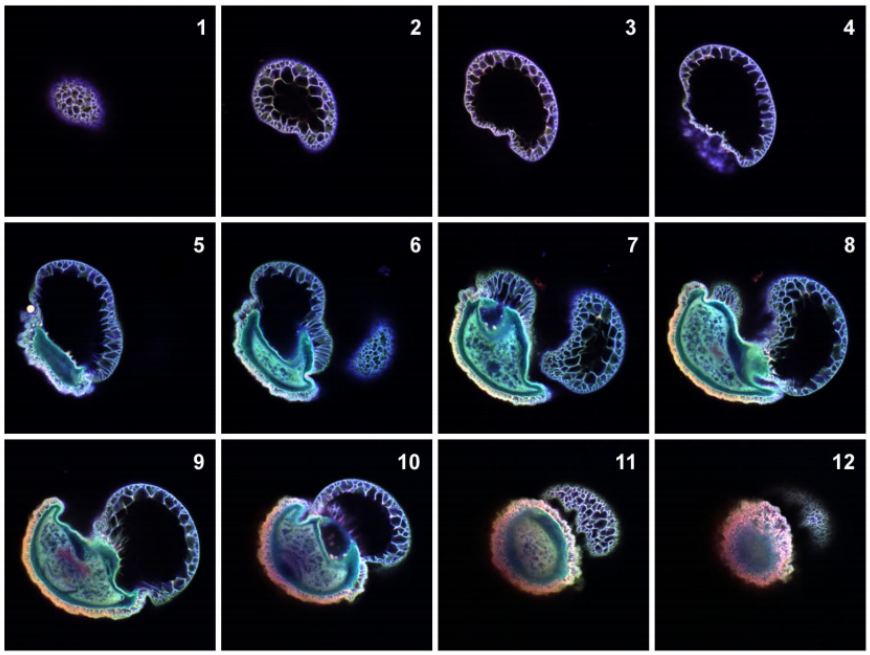

Figure 1.8: Optical sections of *Pinus contorta* pollen. Images is listed sequentially and the axial step size is 3 microns [CFD06]

Theoretically, the field of view of the confocal laser scanning microscope is only dependent on the maximum deflection angle of the scanning mirror. However, in

practice, it is greatly limited by the required scanning frame rate as well as the total scanning time.

There are mainly two drawbacks for this technique. First of all, the scanning process is carried out in 2-dimension (even 3-dimension in some cases), which is painfully time consuming even for a small area. Though the anti-proportional relationship between area of interest and resolution is compromised, the time complexity is now correlated with the spatial bandwidth product (SBP). Secondly, the entire system is bulky, expensive and user-unfriendly. It can easily cost thousands of dollars for each system.

1.3 Holographic microscope

The SBP of the convention microscope is limited by the lens system, since the resolution (magnification) is anti-proportional to the field of view (field number) as shown in Equation 1.6. In order to get rid of the lens system, an possible alternative is holographic microscopy.

Holography as a method to improve the performance of electron microscopes is first proposed by Dénes Gábor in late 1940s [Gab48] [Gab49], which later rewarded him with 1971 Nobel Prize in Physics. The original setups suggested for electron microscopy is provided in Figure 1.9. In [Gab49], he describe the "holography" as a two-step process including "recording" and "reconstruction":

- **Recording**: A coherent illumination beam is first incident onto the object. Then, a small portion of the incident wave $O(x, y, z)$ is diffracted by the object and further interferes with the unscattered part of the original illumination $R(x, y, z)$ (reference beam). The light intensity distribution of the formed fringe patterns $H(x, y, z)$ are then recorded on a photographic plate:

$$
\begin{aligned}
|H(x,y,z=z_0)|^2 &= |R(x,y,z=z_0)+O(x,y,z=z_0)|^2 \\
&= |R(x,y,z=z_0)|^2+|O(x,y,z=z_0)|^2+R^*(x,y,z=z_0) \\
&\quad O(x,y,z=z_0)+O^*(x,y,z=z_0)R(x,y,z=z_0)
\end{aligned} \tag{1.8}
$$

where the first term represents the background produced by the reference beam, the second term is the self interference term, while the last two terms are the holographic terms that carry useful information.

- **Reconstruction**: If the photographic plate is later illuminated by the same reference beam, the resultant field can be described by:

$$
\begin{aligned}
R(x,y,z=z_0)|H(x,y,z=z_0)|^2 &= R(x,y,z=z_0)|R(x,y,z=z_0)|^2 \\
&\quad +R(x,y,z=z_0)|O(x,y,z=z_0)|^2 \\
&\quad +|R(x,y,z=z_0)|^2O(x,y,z=z_0) \\
&\quad +O^*(x,y,z=z_0)R^2(x,y,z=z_0)
\end{aligned} \tag{1.9}
$$

where, the first term is a constant background and the second term is a negligibly small self-interference term. The only useful terms in Equation 1.9 are the third and fourth terms, which represent the original object wave and its complex conjugate.

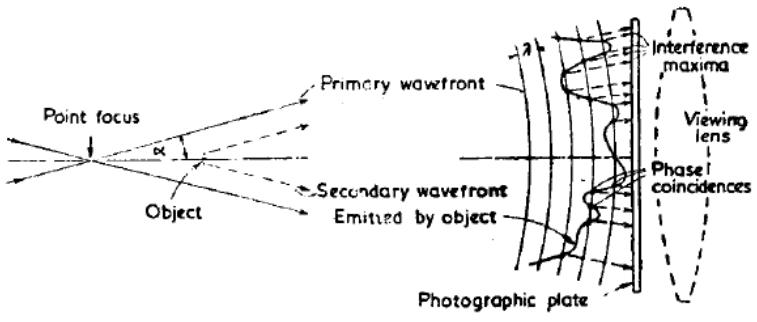

Figure 1.9: Schematic drawing of holographic geometry [Gab48]

Though the original work by Gábor Dénes was intended to improve electron microscope, the underlying principle and experimental configuration can be easily applied to optical domain. Following the invention of LASER (Light Amplification by Stimulated Emission of Radiation) source, Yuri Denisyuk in the Soviet Union [Den62] and Emmett Leith and Juris Upatnieks [LU62] in United States succeeded in presenting the first practical optical holograms in 1962, independently. After that, different kinds of optical holography emerged, including transmission hologram [LU62], reflection hologram [Den62], "rainbow transmission hologram" [Ben69], and "volume hologram" [Rus81].

1.3.1 Digital holographic microscopy

As first suggested by Joseph W. Goodman in 1967 [GL67] and later experimentally presented by Schnar and Jüptner on CCD-based image sensor in 1994 [SJ94], digital holography quickly became a very important technique in the field of microscopy; it can provide not only the intensity information of the object but also the phase information. Compared to its analog counterpart, the digital holography is slightly different in two aspects.

- Uses opto-electronic devices, such as charge-coupled device (CCD), Complementary metal-oxide-semiconductor (CMOS), or photomultiplier tubes (PMTs) instead of conventional photographic plates to capture the interference fringes. The hologram is stored in digital format.
- In the "reconstruction stage", digital computer are used to numerically simulate the process; the propagation of the diffraction pattern in free space is calculated. The resultant image is also rendered digitally on screens or monitors.

Digital in-line holographic microscopy with coherent spherical wavefront illumination was presented by Kreuzer Group [GXJ06]. The system takes advantage

of a pinhole (P), whose size is equivalent with the wavelength of the illumination, to generate a coherent spherical wavefront (Figure 1.10). Then, after going through the pinhole, the focused laser beam (L) will shine the object (O) and the hologram is formed and detected by the image sensors (C). Since the distance (z_1) between the object and pinhole is much smaller than that (z_2) between the sensors and pinhole, the hologram is magnified by a factor of $1 + z_2/z_1$.

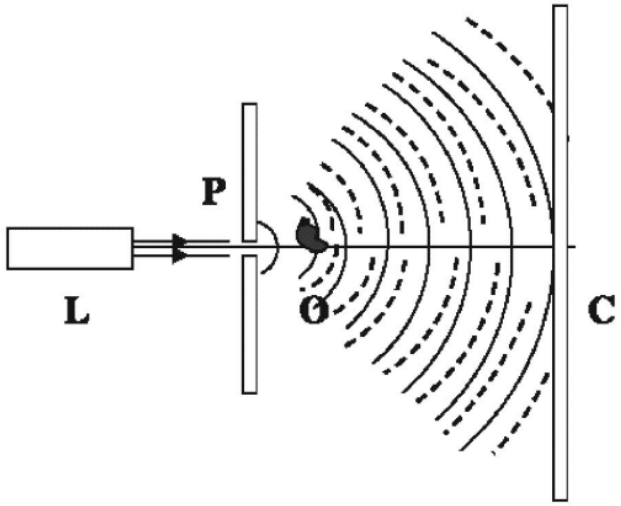

Figure 1.10: System configuration for digital in-line holographic microscopy [GXJ06]

However, even for the state-of-art computers, the computational burden of propagating hologram of a large size is still considerably heavy. Therefore, many numerical methods are invented to reconstruct the digital holograms. One of the most important methods is by applying Kirchhoff-Fresnel transformation to reconstruct high NA holograms [Bar88]. Kruezer group later improved this method by further transforming the hologram to spherical coordinate system [Kre02]. Based on this technique, Kanka recently came up with a proposal to cope with the aliasing problem for the spherical wave, which made the more rigorous angular spectrum method possible [KRK09].

1.4 Our group's previous work on lensfree microscopy

In the past five years, our laboratory, Nano- and Bio-Photonics Laboratory at UCLA, has been striving to develop novel imaging systems that enjoy characteristics such as compact, low-cost, and lens-free, which can address the immediate needs and requirements of telemedicine for global health problems. In the following subsections, several techniques we have developed in our lab will be discussed in details.

1.4.1 Lensless, Ultra wide-field Cell monitoring array platform based on shadow imaging (LUCAS)

Rather than competing with other microscopic modality, the first version of LUCAS platform was aiming for on-chip cells counting problem, especially for the microfluidic devices [OD08]. The field of view of the system is $\sim$10 cm^2. A sketch of the system configuration is provided in Figure 1.11. The cells are placed between two microscope slides, while the sensor array are placed under the slides.

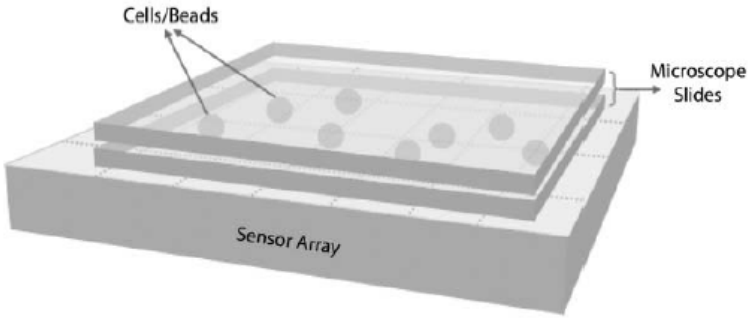

Figure 1.11: A simplified sketch of LUCAS system. [OD08]

However, for the shadow imaging system, the largest issue is imposed by the density of the sample. As we can see from Figure 1.12, the diameter of the shadow is slightly larger than that of the object. Therefore, a very dense sample might

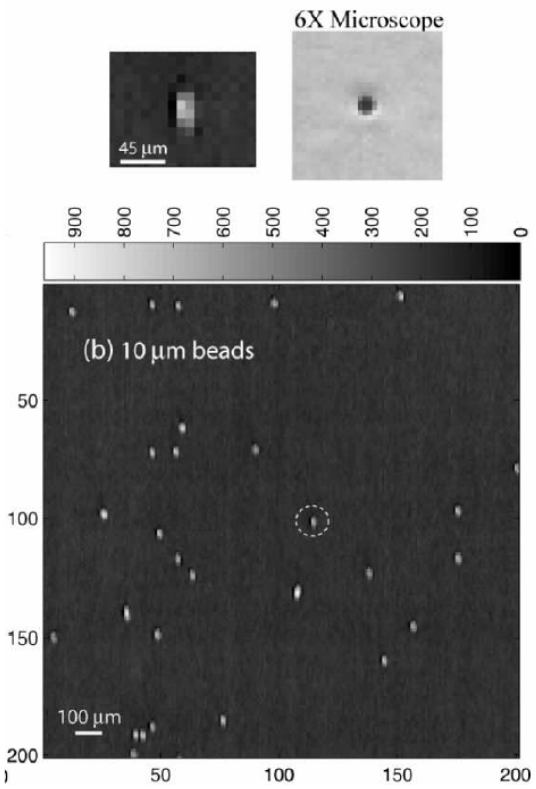

Figure 1.12: LUCAS image of 10 μm polystyrene microbeads. [OD08]

give rise to the errors when an automatic pattern recognition algorithm is applied to count the number of the cells. Also, the specificity of the system is limited, since the diffraction pattern of the sample is not completely consistent in bright field.

1.4.2 Holographic-LUCAS

In order to improve the performance of LUCAS system, a holographic version was proposed in [SST09]. By replacing the spatially incoherent broadband white-light illumination with a spatially coherent monochromator, we managed to record the holographic diffraction signature of the object instead of the incoherent diffraction pattern. The schematic drawing of the system are presented in Figure 1.13.

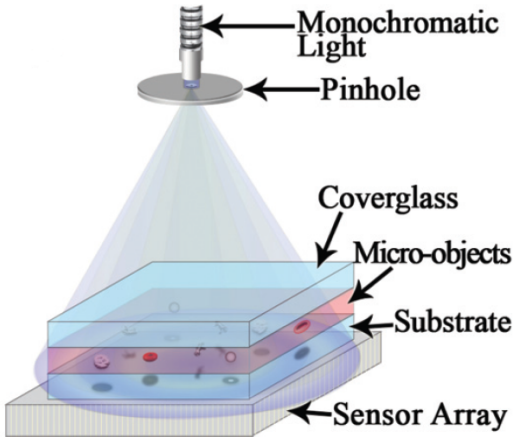

Figure 1.13: Schematic diagram of holographic LUCAS system. [SST09]

This modification brought us several benefits, including the improved signal-to-noise ratio (SNR) and more consistent signature. The following Figure 1.14 illustrates the performance enhancement of the platform.

Another follow-up research in this direction is carried out and presented in 2010. Rather than merely studying the raw holographic signatures, a further step, digital reconstruction of the hologram, was taken to provide the researcher with

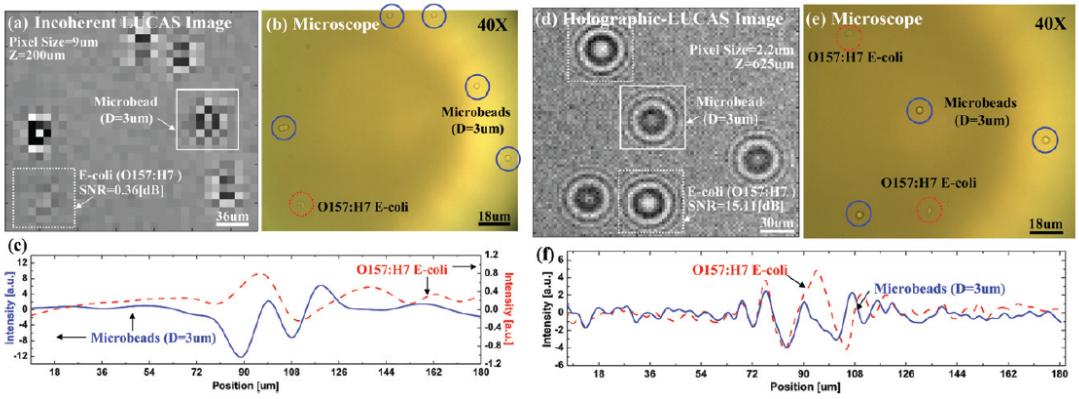

Figure 1.14: (a) LUCAS image, (b) microscope comparison, (c) cross profile of a heterogeneous sample of 3μm micro beads and *E. coli* sample by using 9μm pixel size sensor array. (d) Holographic-LUCAS image, (e) microscope comparison, (f) cross profile of a heterogeneous sample of 3μm micro beads and E. coli sample by using 2.2μm pixel size sensor array. [SST09]

a more intuitive microscopic images of the object [ISM10]. In this study, color and monochrome digital reconstruction of the holograms of the *Caenorhabditis elegans* is performed by using the on-chip Holographic-LUCAS system mentioned beforehand. The experimental results are presented in the following Figure 1.15.

The optical system used here should not be confused with that shown in Figure 1.10: z_1 in this case is much larger than the z_2. This significant difference results in several unique features:

- *Larger field of view*: since the fringe magnification is $\sim$1, the field of view is the same as the size of the image sensors.

- *Planar wavefront*: instead of the spherical wavefront due to the larger z_1. Therefore, the sampling and aliasing related issues related to spherical wavefront as mentioned before can be avoided.

- *Lower requirements on spatial and temporal coherence of the light source*: the

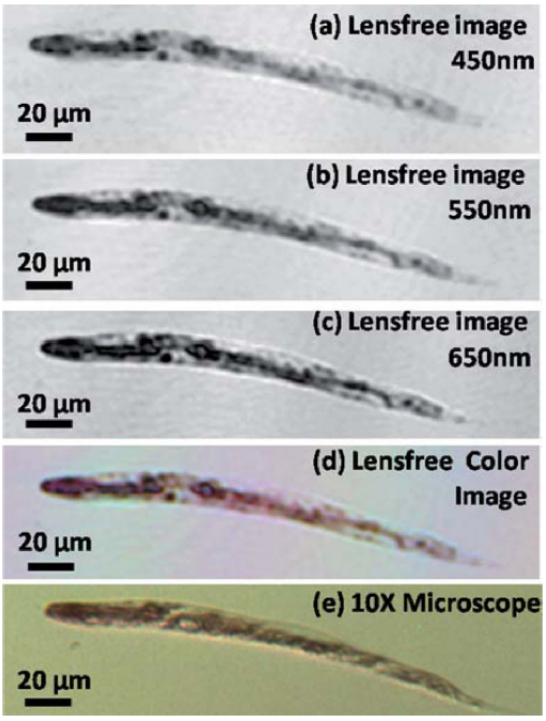

Figure 1.15: Digitally reconstructed holographic images of a stained *C. elegans* sample using Ponceau S red stain, captured with illumination wavelengths at (a) 450 nm, (b) 550 nm, (c) 650 nm. (d) Fused color image and (e) 10× microscopic comparison [ISM10]

pinhole used in this setup is much larger than that in Kreuzer's, therefore it can be viewed as a partially coherent illumination, or, in other words, locally coherent illumination as long as the size of the object of interest is smaller than the spatial coherent diameter in the detector plane. This means that simpler and cheaper light sources such as LEDs can be used instead of carefully coupled lasers.

1.4.3 Fluorescent-LUCAS

Aiming for high-throughput screening problems, such as rare cell detection, our group presented another imaging modality based on fluorescent imaging technique. The schematic drawing of the system is given in Figure 1.16

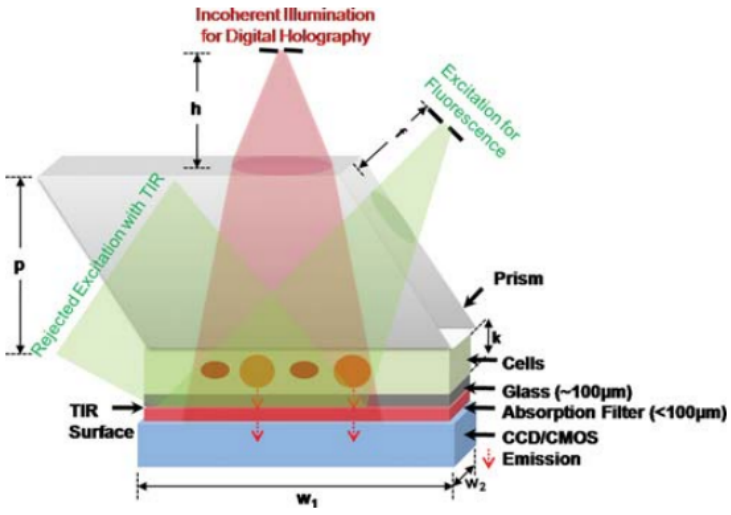

Figure 1.16: Schematic diagram of fluorescent LUCAS system. [CSO10]

By inserting a Total Internal Reflection (TIR) surface between the sample and the detector, the excitation light is reflected, while the emission light from the fluorescent sample can still penetrate the TIR layer. This is because that the incident angle of the illumination is usually made larger than the critical angle,

but the re-emitted light from the fluorescent sample is uniformly distributed in angular space and hence the re-emitted light no longer obeys the TIR condition. In addition, another cheap absorption filter can be placed to further enhance the contrast ratio of the system.

Meanwhile, post processing on the image such digital deconvolution proved to be able to further improve the spatial resolution of the system as shown in Figure 1.17

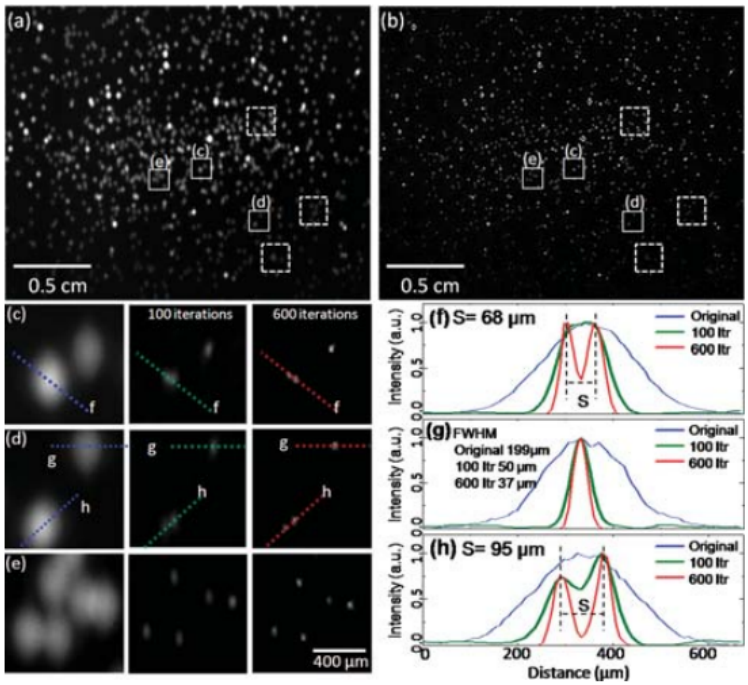

Figure 1.17: (a) Raw (b) deconvolved fluorescent lensfree image of 10μm microbeads. (c-e) comparison between the cropped raw images and their deconvolved counterparts. (f-h) cross profile of the microbeads between raw images and deconvolved counterparts. [CSO10]

1.5 Motivation of this project

As we have discussed in previous section, the LUCAS platform enjoys a very large field of view (FOV), in comparison with conventional optical microscopes. Unfortunately, in some biological settings, this is simply not enough. For example, for the detection of circulating tumor cells (CTC), whose concentration can be as low as 1-10 CTC per mL, the LUCAS system might experience some difficulties. Therefore, it is necessary for us to develop a modality that can handle this problem.

Since the FOV of LUCAS system is actually limited by the size of the image sensor array, a natural thought is then to adopt the scanning mechanism. Therefore, in order to keep the design simple and low-cost, we turn to the commercial flatbed scanner.

By modifying a commercial flatbed scanner in the terms of software control, illumination configuration, and optical setups, we can covert it to a biomedical imaging system, whose screening capability of the system can be up to 8 mL according to our calculations; the the active area of a commercial scanner is as huge as 600 cm^2 (for letter paper), while the height of the opto-fluidic chamber can be made to 130 μm. Therefore, the proposed system will be an ideal candidate for ultra field-of-view cytometry application and rare cell detections.

1.5.1 Related works

Recently, Guoan Zheng et al. has proposed a gigapixel imaging system based on a commercially available closed-circuit-television (CCTV) lens system and a flatbed scanner [ZOY12]. Their setups are sketched in Figure 1.18

By adopting a CCTV lens as mentioned above, the entire system possess a magnification factor of $\sim$30. Therefore, the resulted compound system boosts the original resolution of the flatbed scanner from 2400 dpi (10 μm) up to $\sim$0.7μm.

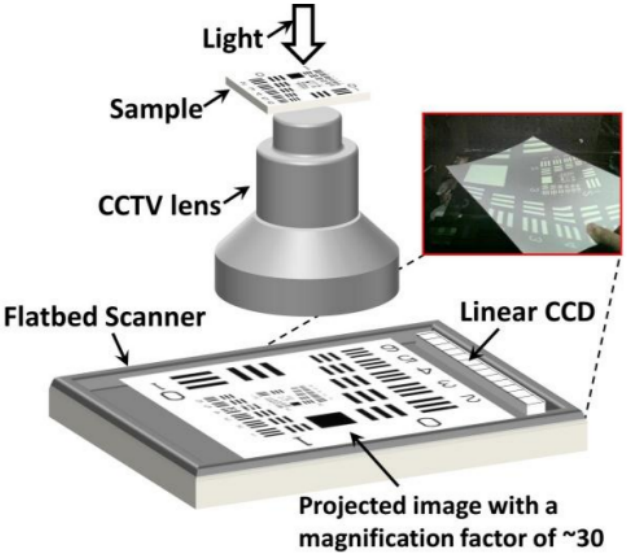

Figure 1.18: The setup of the proposed 0.54 gigapixel microscopy. [ZOY12]

However, on the other hand, the actual FOV of the system is shrinking from 29.7cm×21.6 down to merely 1cm×0.75cm. Moreover, an automatic focusing algorithm is applied to further improve the quality of the image.

There are other literatures that mentioned the usage of flatbed scanner. Fox et al. proposed that the flatbed scanner could be used as a simple tool for human skeleton [FEM11]. Flatbed scanner is also mentioned in the applications such as immunoassay characterization [YHC09] and virus plaque quantitation [SKQ12].

However, one should be aware that all of the above just use the scanner as it is. No further modifications on either the operating mechanism or optical configuration of the scanner were made.

CHAPTER 2

Hardware and optical configurations

The schematic drawing of the proposed system is shown in Figure 2.1,

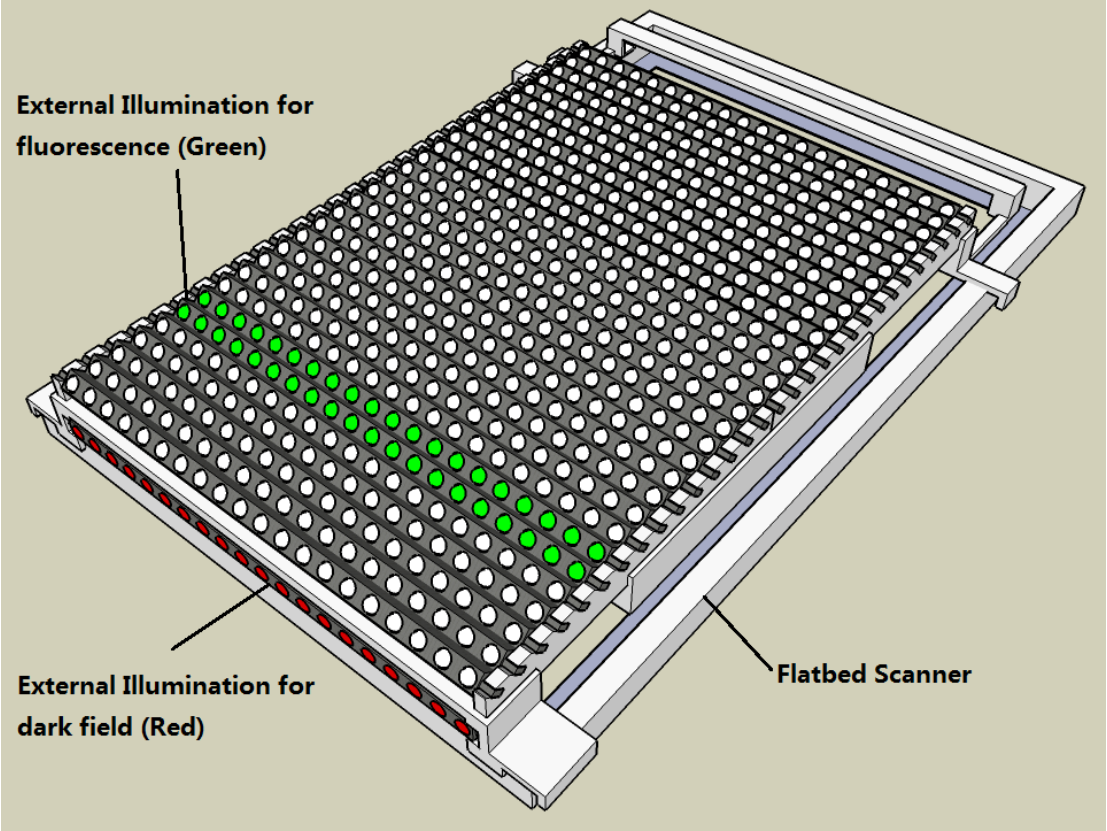

Figure 2.1: Schematic diagram of scanner system.

The entire system can be divided into three parts: flatbed scanner, external illuminations for dark field imaging, and external illumination for fluorescent imaging. Each part of the system will be explained in details in the following sections.

2.1 Scanner: Canon CanoScan LiDE 200F

As one of the core components of the system, the scanner is responsible for forming an image of the sample in the image plane and recording the intensity distribution of the resultant light field. After capturing the images, the scanner will package the data and transfer them to the host computer. All the information of the image will then be kept in digital format. In our system, Contact Image Sensor (CIS) technology is applied and will be discussed in details in the following section.

2.1.1 Optics in the scanner

In our project, we selected Canon CanoScan LiDE 200F with CIS technology, which is claimed to be capable of scanning a document at 4800 dpi by using internal reflective illumination, while providing a bit depth of 16 bits/pixel for grayscale imaging.

CIS technology uses monochromatic CMOS devices as photodetectors and the structure of the system is shown in Figure 2.2. In this case, the illumination unit, which is usually made up of RGB tricolor LEDs, is moving with the CMOS linear sensor array. An array of Selfoc lens is placed on the top of the CMOS linear sensor array. The tricolor LEDs are time-sequentially flash during the scanning process, while the grayscale CMOS image sensor is collecting the reflected image formed by the Selfoc Lens Array (SLA).

One of the most essential components of the CIS scanner system is the SLA, which is a linear array of gradient-index fiber array. SLA can form a unit magnified and erect image of the object as shwon in Figure 2.3 [KO80].

The image formation through SLA can be viewed as a weighted superposition of several copies of the original object via different lens elements. We will only achieve a perfectly overlaid image, if we carefully align those lenses and put the detector right on the focal plane. Otherwise, the misalignment will result in

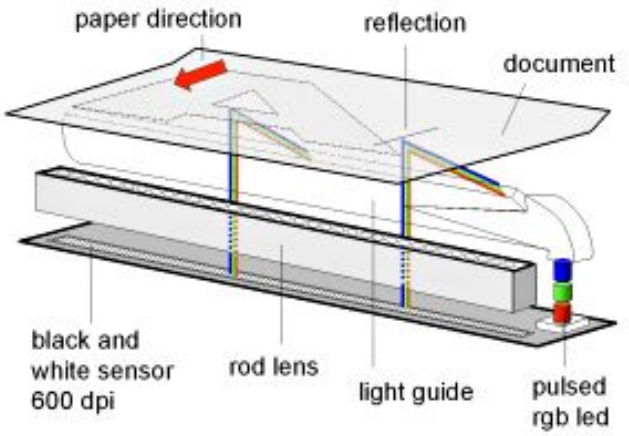

Figure 2.2: CIS technology.

`http://www.canon-compo.co.jp/e/technology/cis.html`

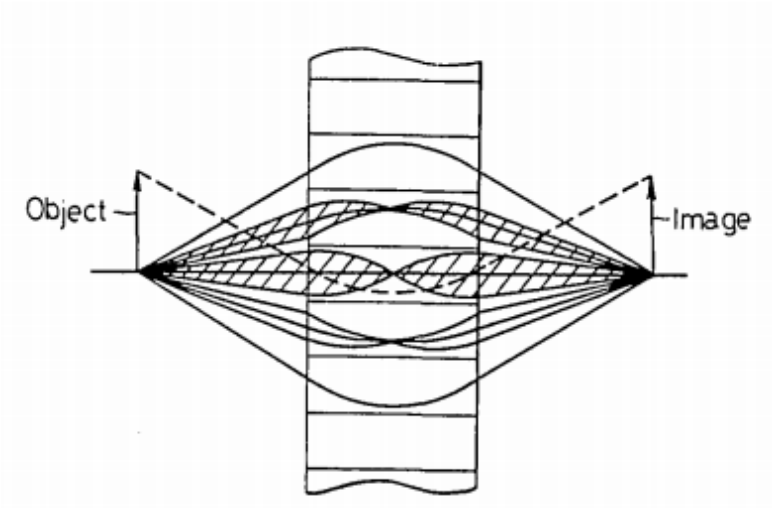

Figure 2.3: Lens array image formation [KO80]

Table 2.1: Technical specifications for SLA

SLA Type	No. of Rows	TC (mm)	Lens Diam. (mm)
20D	1	9.1	0.563
Z (mm)	L (mm)	X_0 (mm)	X (mm)
4.30	2.40	0.98	1.96
F-Number	Uniformity ΔI (%)	Wavelength (nm)	Chromatic Aberration
1.35	20.0	570	4.1×10^{-2}

blurred image and impair the resolution of the imaging system.

The scanner chip used in this scanner is Genesys Logic's GL847, while the lens array is SLA-20D, which is manufactured by Nippon Sheet Glass Co., Ltd. The data sheet of this product is listed in Table 2.1. [GoF12]

2.1.2 Modification

By studying the SLA, we found an interesting phenomenon that can be exploited to provide better image contrast; due to the limited NA, the acceptance angle Θ of the lenslet is finite as shown in Figure 2.5, and the incoming light rays, whose incident angles are larger than the acceptance angle, will not be focused.

However, if we put a small particle right on the top of the object plane, the whole story will be changed. Since small particles (1 μm$\sim$ 10μm) will scatter light when they interact with incident light, the direction of the original incident light will be altered by the particles. Considering that the angle of the scattered light ray is uniformly distributed in the angular domain, there will always be a part of the scattered light whose incident angle is smaller than the acceptance angle and hence will be focused by the SLA.

In our case, since the CMOS sensors in the scanner only extend in the sub-scanning direction and is very short in the main-scanning direction (less than 20

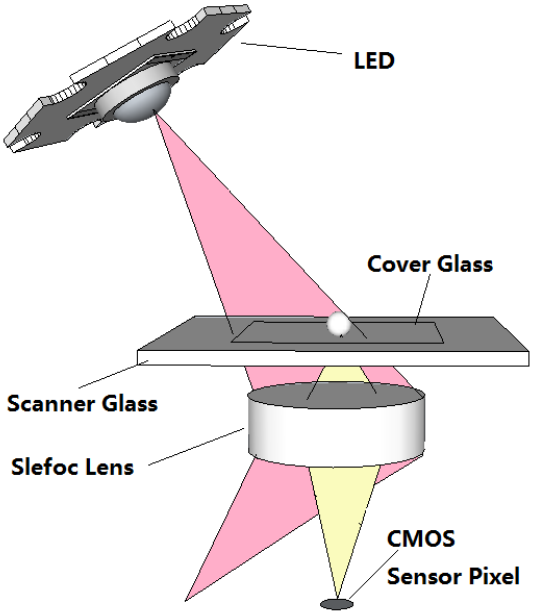

Figure 2.4: Dark field setups. (Not to scale)

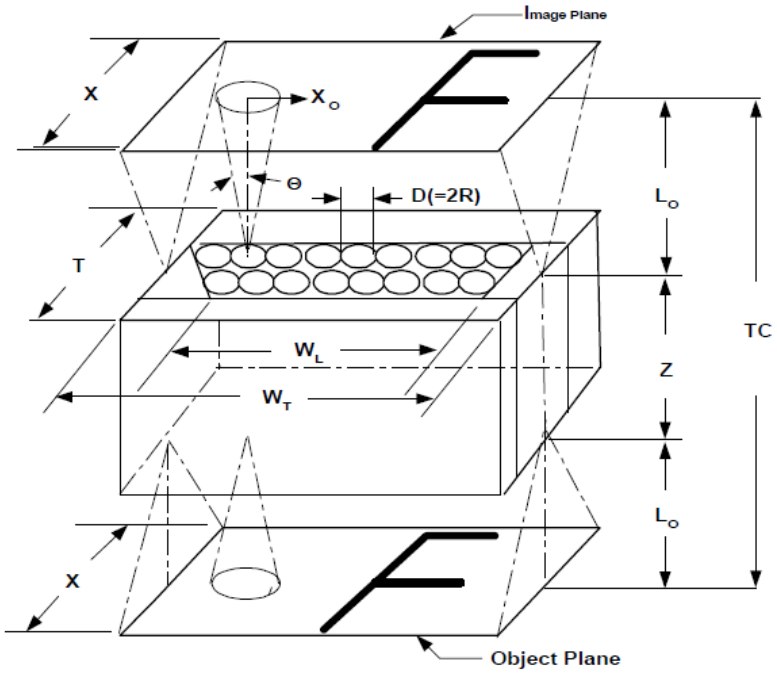

Figure 2.5: SLA dimension parameters. [TAO12]

μm). As a result, the actual "acceptance angle" of the imaging system in the main-scanning direction is much smaller than that of the lens array, because some of incident light ray that falls within the "acceptance" range, and is focused by the lens array, will not be collected by the pixels due to their small active area. Therefore, if we put small particles on the object plane, only the light scattered by the particles will be collected by the linear CMOS sensor array, while all the background illumination will be excluded from the image. The resulted image shows much better contrast (Figure 2.6).

2.2 External illumination

The scanner's internal illumination is really weak; it is only $\sim 2\mu$W, if we measure the light intensity right in the object plane. This amount of light intensity might be enough for normal office use such as document scanning. However, for the object of our interest like micro-beads, or blood cells, this low intensity will be problematic. More importantly, for fluorescence application, the fluorophore will not be able to be excited. So, it is plausible for us to build our own external illumination.

2.2.1 Design: fluorescence and "dark field"

For fluorescence imaging, the illumination should be spatially well confined so as not to photobleach the fluorophores or excite too many fluorophores simultaneously. Nonetheless, the intensity of the illumination should be strong enough to excite the fluorescent emission. Therefore, the best solution is to use a light source that can move along with the sensor array; there will be only a small proportion of the sample is illuminated at a time when the scanner is scanning. We are currently using multiple linear arrays of LEDs and sequentially switching them on and off to follow the sensor array, instead of using a movable linear arrays of LEDs, as

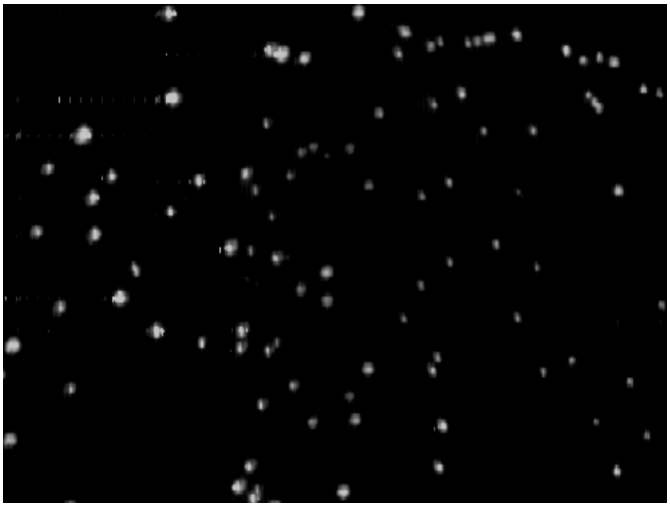

(a)

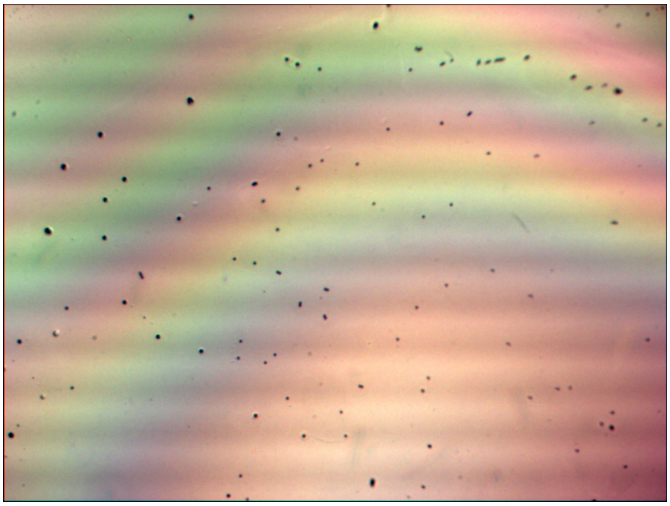

(b)

Figure 2.6: (a) Dark field image, (b) microscope comparison of 10μm microbeads

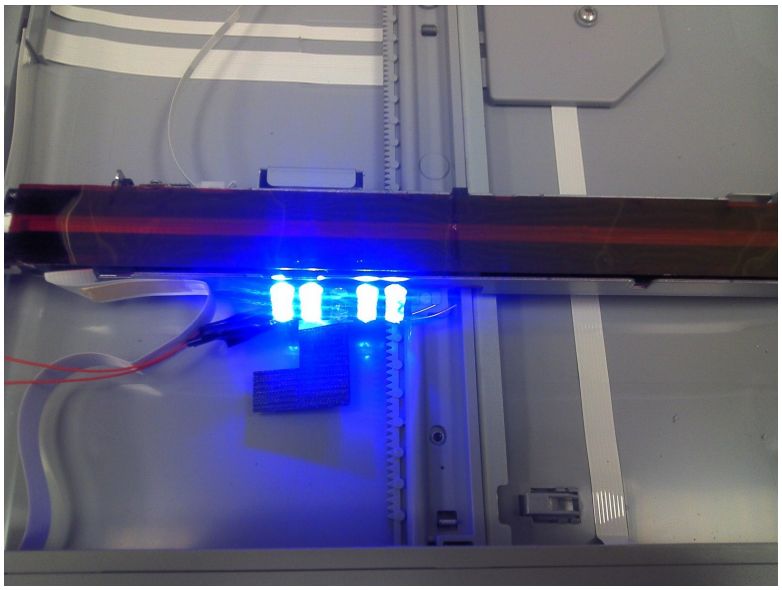

Figure 2.7: Integrated external fluorescent illumination (proof of principle)

illustrated in Figure 2.1. In this configuration, the control signal is sent from the host computer based on the line counter of output image, which will be discussed in later chapter. In the meantime, we are also investigating the possibility of integrating external illumination with the scanner head (Figure 2.7). However, the drawback of this scheme is that the field of view will be compromised and almost half of the light coming from the illumination will not reach the sample.

In the meantime, another set of linear LED arrays are dedicated to the "dark field" imaging, which is also described in Figure 2.1

2.2.2 Circuits

In order to obtain uniform illumination on the scanned object in fluorescent mode, we need to sequentially turn on the green LED array row by row. Two rows are simultaneously switched on to illuminate the area that is being scanned. As to dark field, two rows of red LEDs are simultaneously illuminating the sample from

front and back side to ensure the uniformity.

Then, we came up with an implementation based on Aduino board. An analog circuit interface is built to bridge the scanner driver and LED array by using power switches, voltage regulators, and a microcontroller (Aduino board). The microcontroller continuously decodes binary inputs sent from scanner driver and turns on the corresponding power switches, and further switches on the corresponding rows of LEDs. Furthermore, a potentiometer allows adjustable light intensity. The PCB board and circuits are shown in Figure 2.8.

The flow chart of illumination control system is provided (Figure 2.9). More detailed descriptions of the locating algorithm (to locate the position of the scanner head) will be discussed in later chapters.

2.3 Filter

One of the most influential factors that controls the quality of the fluorescent image is the quality of the filters, i.e. excitation filter and emission filter. The excitation filter usually has a very short passband, which ensures that the transmitted illumination is nearly monochromatic at the correct wavelength. To the contrary, the transmission spectrum of the emission filter should include the entire emission spectrum to increase the SNR, while excluding the illumination spectrum. Moreover, emission filter's spectrum should have a sharp cut-off to prevent crosstalk between the illumination background and fluorescent signal.

Generally, there are three types of filters that we can choose from: interferometric filter, Roscolux (polycarbonate and polyester) filter and Orasol dye filter. The spectra of these filters are shown in Figure 2.10. The performance of the interferometric filter is the best among them, while the dye filter performs better than the Roscolux filter in terms of the sharpness of the cutoff as well as the transmission of the passband.

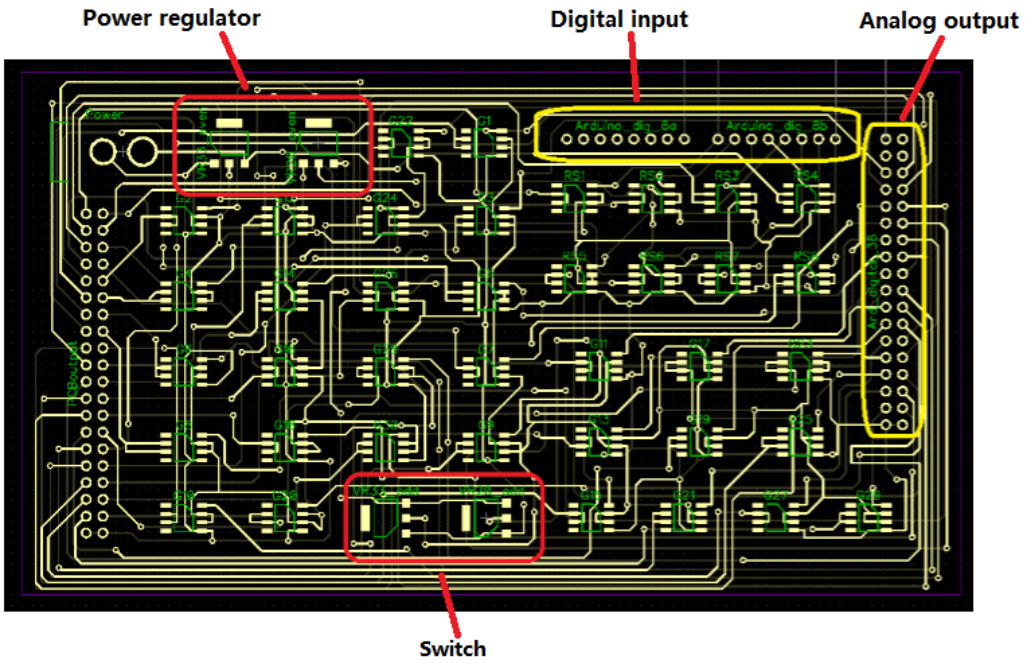

(a)

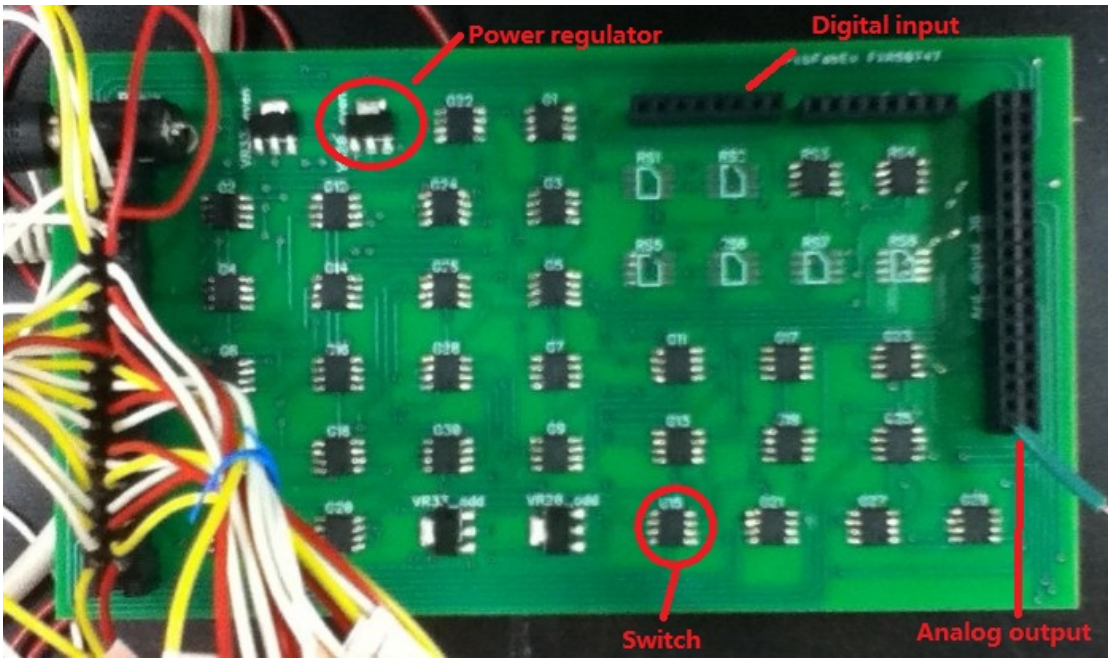

(b)

Figure 2.8: (a) Schematic diagram, (b) actual picture of the switching board.

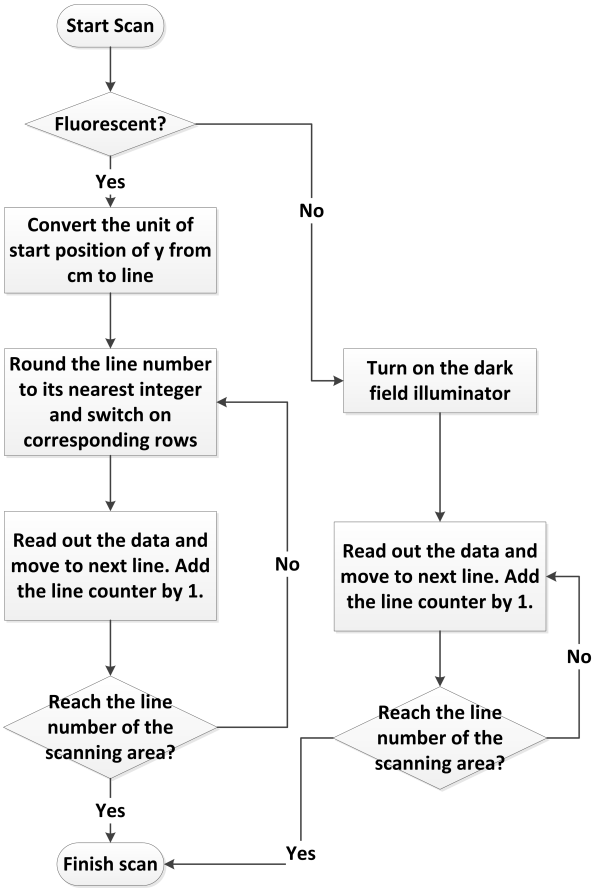

Figure 2.9: Flow chart of scanner head locating algorithm

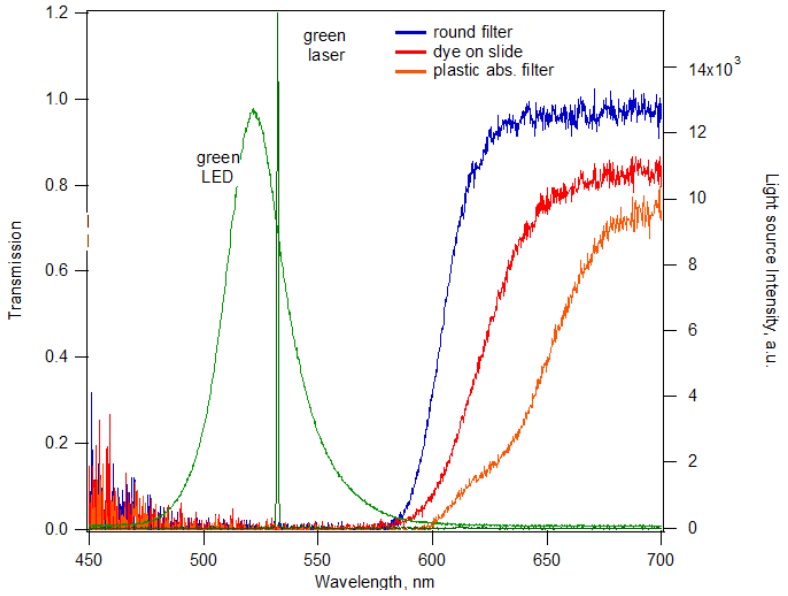

Figure 2.10: Spectral comparison among interferometric filter, Roscolux filter and dye filters

The filter can be inserted in two places: either above the scanner glass or in front of the Selfoc Lens Array. For the first option, it is difficult to make an good interferometric filter or dye filter over such a large area by their conventional fabrication process. For example, the fabrication of the interferometric filter is carried out by using vacuum deposition system, while that of the dye filter is done by either spinning coating or solution casting. But in our case, we cannot apply those procedures to our scanner system directly, because the scanner glass is much larger than the commonly used chamber for vacuum deposition and spin coating systems. Additionally, it is also challenging for us to create a uniform coating over such a large area ($\sim$600 cm^2). For the latter option, we can simply fabricate a stripe filter and cover the lens array with it.

Since the interferometric filter is very expensive even for a small area, two other cheaper alternatives are used and tested in this project: commercially available Roscolux filter and fabricated dye filter. For the fabrication of orasol dye filter,

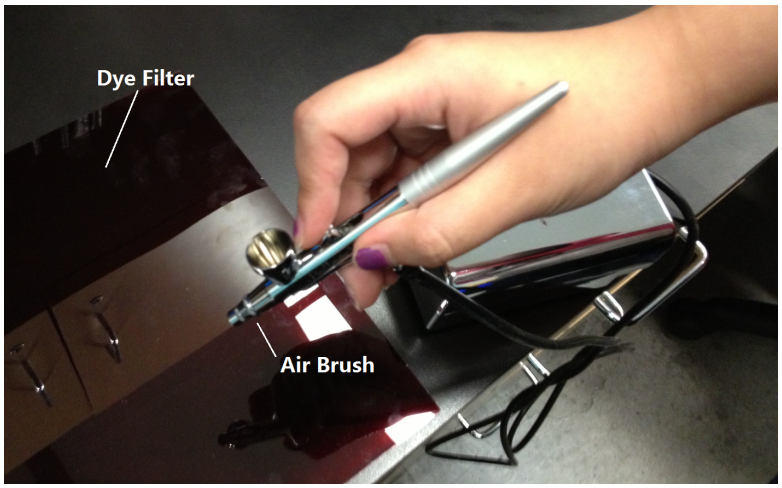

Figure 2.11: Spray coating with air brush

several attempts have been made based on different fabrication method and recipe.

2.3.1 Spray coating

Spray coating is widely adopted in polymer material deposition for its simplicity [Kre09]. By forcing the solution through a nozzle to form a fine aerosol, the technique enables the coating at the object surface. However, the formation of the aerosol and the following evaporation of the solvent are very complex, it is difficult to fabricate a smooth surface even for a small area. Nonetheless, the technique still remain its value due to its simple sample preparation and coating process.

In our case, a cosmetic air brush is used to spray the Orasol dye dissolved in cyclonepantanon solution onto the mylar sheet, which has already been gone through the surface treatment (Figure 2.11). The resultant sheet shows small holes all over the place and the thinkness distribution is also not satisfactory.

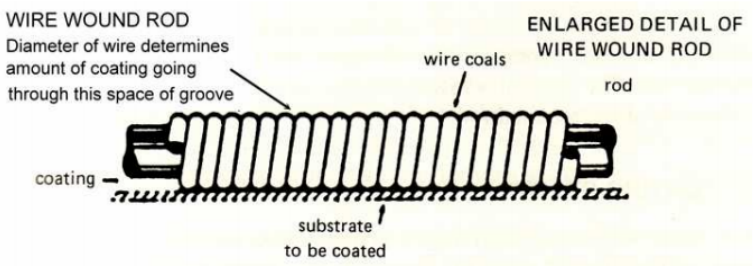

Figure 2.12: Wire wound coating rod [Rod]

2.3.2 Rod coating

The wire-wound metering rod coating method was invented by Charles W. Mayer in early 20^{th} century, so it is also widely know as Mayer rod. A typical coating rod is shown in Figure 2.12 [Rod]. For this technique, the thickness of the wet film is determined by the diameter of the wire. In this study, we have tried two rods with different wire diameter: 7 μm and 10 μm. Several different recipes were also used for rod coating as listed below and the resultant spectra are shown in Figure 2.13.

- Ethanol + dye: cracked and scratched over time
- Cyclopentanone + dye [CSS11] [RRA09]:
  - the transmission curve fitted the need
  - holes on the surface after coating
- MTMS + TEOS + dye:
  - Uniform coating, but destroyed the spectral transmission curve

Currently, we are using dye filter that is rod coated by cyclopentanone solution. After coating a large area, only a small stripe is cut off and used to cover the lens array as shown in 2.12.

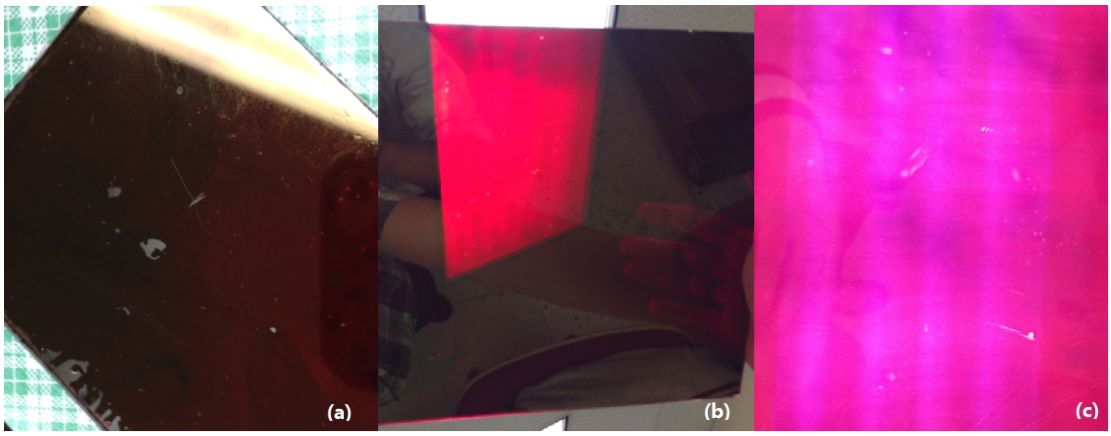

Figure 2.13: Dye filter fabricated with different solvents (a) Ethanol (b) Cyclopentanone (c) MTMS + TEOS

2.4 Micro-fluidic chamber

Microfluidic devices have been widely used in flow cytometer for cell counting or sorting application [KSO02]. However, due to the limitation placed by the conventional optical microscope, the observation volume for undiluted whole blood samples is typically less than 0.2-0.3 μL [AAC12]. In this project, the proposed scanner platform is used to evaluate the microfluidic chamber with fluorescent beads in whole blood.

2.4.0.1 Fabrication

The fabrication of the chamber is described as follows: 1 mm thick microscope slide (50 mm by 75 mm), a 150 μm thick cover glass (45 mm by 60 mm), super thin (130 μm) double-side adhesive tape, and a tygon tube of inner diameter of 0.5mm are used to create the chamber. Two holes, one of 1 mm diameter and another of 2 mm diameter at 40 mm apart from each other, are drilled along the center line of the 1 mm glass. The larger hole is intended for tube insertion and the smaller hole is intended to let air out of the chamber during the filling process.

Figure 2.14: Microfluidic chamber.

The 130 mum adhesive layer is cut into a hexagonal shaped frame and is used to glue the boundaries of the two glasses together, leaving the middle section empty as the chamber space. A tube is then inserted into the larger hole on the 1 mm microscope slide and fixed with epoxy. The chamber is then ready to use (Figure 2.14).

2.5 Fluidic microlens formed on nano particles

In a recent article [MML13], a self-assembled fluidic microlens technique is adopted to increase the light intensity of the fluorescent microbeads. The same technique is applied in our study to enhance the detection sensitivity of our scanner platform.

2.5.1 Fluidic microlens sample preparation

The sample of interest (in our case the fluorescent microbeads) is diluted with the TRIS -PEG solution (0.1 M TRIS-HCl pH 8.0 C 10% PEG 600) to the desired concentration. A cleaned cover glass is treated with the high frequency generator for two minutes, making the glass surface hydrophilic. A small amount (for instance 2 μL over 1cm^2 cover glass) of the sample solution is transferred to the center of the cover glass. The reaction between the TRIS-PEG solution and the hydrophilic surface will cause the sample to move around on the cover glass. Try to stabilize the sample by tilting the cover glass. Once the sample is stabilized around the center of the glass, allow it to sit for five minutes so that the sample can settle and stick to the cover glass. Then slightly tilt the cover glass so the solution slides off slowly, leaving the sample with fluidic microlens on the cover glass.

CHAPTER 3

Control program of the scanner

3.1 Introduction and objectives

As discussed in the previous chapter (Figure 2.1), the flatbed scanner plays an important role in the proposed imaging system. Its functionalities are similar to that of the conventional CCD or CMOS sensor inside the digital camera. There emerges an instant need to set the parameters for imaging, such as exposure time, gain and offset of the A/D converter, bit depth, and active area. More importantly, we need to obtain the access to the raw data of the image to eliminate the unnecessary errors coming from the post processing procedures performed by the scanner chip.

However, most flatbed scanners are designed to scan documents. The default scanner softwares usually do not offer the raw data. We need to purchase third party softwares such as VueScan to obtain the raw data. As to other parameters we mentioned above, none of the commercially available software is capable of tuning them. Therefore, we have to come up with our own solution.

Fortunately, there is an open-source project called Scanner Access Now Easy (SANE) available for Linux operating system, which provides generic application programming interface (API) for developers over a range of raster scanner devices. We can take advantage of the existing routines defined in the SANE backend to gain the access to the scanner chip's registers and thus directly override the default settings at will.

At last, we should be able to fulfill the following objectives:

- Obtain raw data for different channels (RGB) from the monochromatic imager
- Turn off the internal illumination.
- Set the optical resolution, interest of area.
- Set the parameters for analog-digital converter (ADC), such as offset and gain.
- Set the parameters for contact image sensor (CIS), such as exposure time, gain, and gain factor for different channel
- Set the parameters for motor movement, such as line period (moving speed), acceleration, deceleration speed.

3.2 The hierarchy of the scanner control program

Before working on implementing our own control program, let's first take a close look at how the default software works. As we can see from Figure 3.1, the scanner control hierarchy can be roughly divided into four layers. On the top layer, the user is responsible for setting the options and parameters of interest. Then, the frontend application will translate those options or parameters into corresponding register values and send them to the device driver through preset API. In the next level, the device driver will package those commands, and stream them to the hardware via USB connection. Upon receiving the data stream, the scanner chip will then send the command to different subsystems correspondingly based on the decoding results of the registers' values as illustrated in Figure 3.2. Finally, the required action will be performed. In the following subsections, I will provide a detailed explanation of each layer.

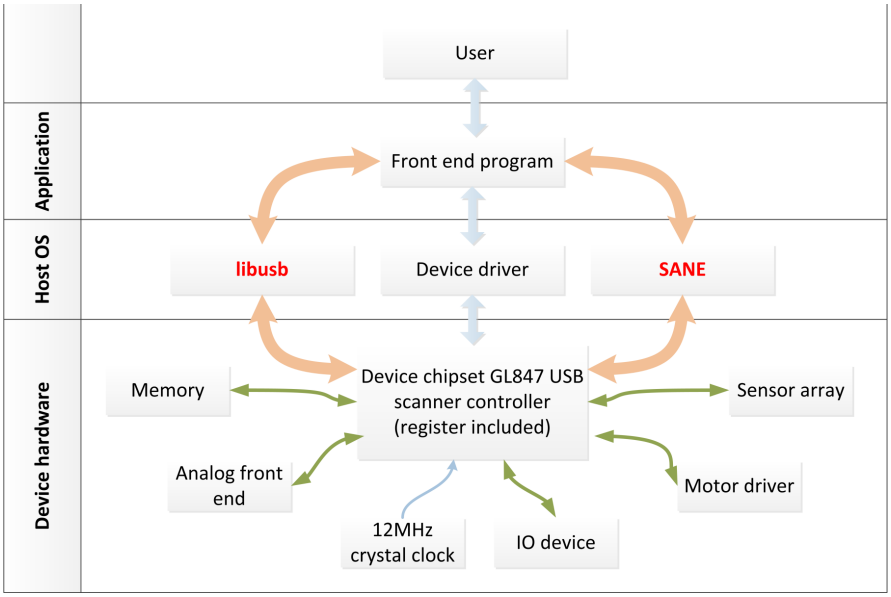

Figure 3.1: The hierarchy Of the scanner control program

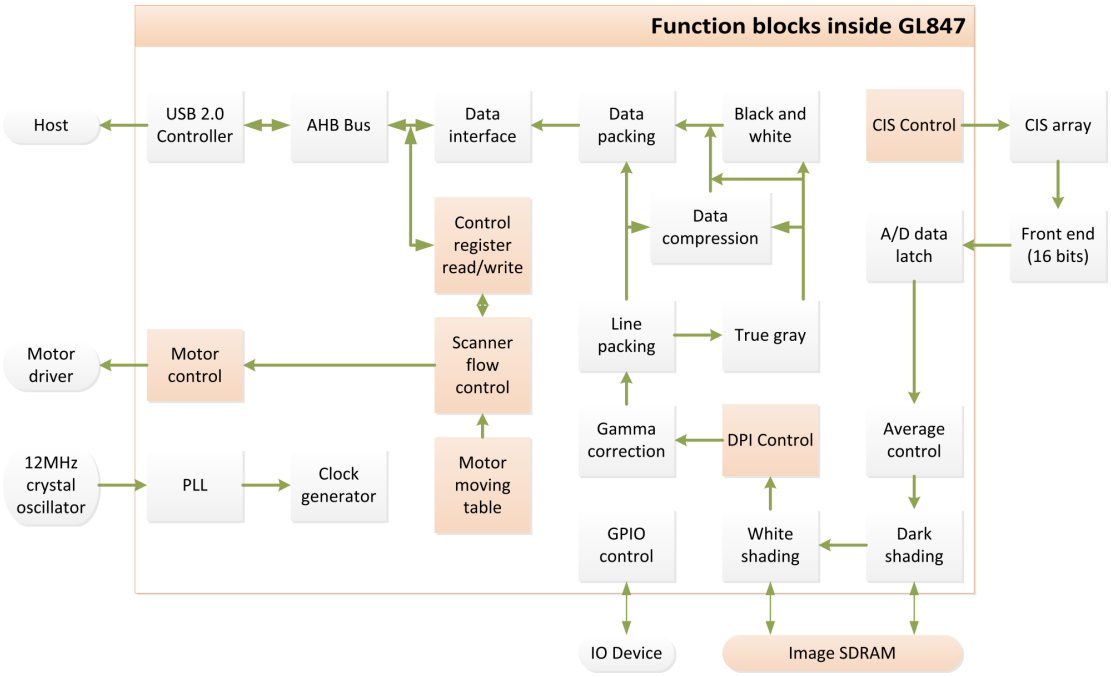

Figure 3.2: Working flow chart and internal function blocks of GL847 chipset

3.2.1 Device hardware

The scanner, Canon CanoScan LiDE 200F, applies Genesys Logic's GL847 scanner chip as its central controller. The chip integrates both the scanner function application-specific integrated circuit (ASIC) and the USB 2.0 interface controller. Please be noted that I actually refer to GL846's datasheet throughout the project, since the technical details of GL847 are currently unavailable and the specifications and functionalities of those two models are almost the same.

According to the datasheet, the scanner control on the device level is achieved by assigning different values to the scanner registers. The total number of the registers in the scanner is 256, and each of them is 8 bits long. Each byte or bit of them corresponds to a specific scanner status or parameter. For example, by designating different values to the second bit of the register 0x04, the user can define the BITSET to be either 1 or 0. Then, the scanner chip will decode it. If BITSET is set to be 1, one pixel of the image will be one word long. Otherwise, one pixel of the image will be only one byte long.

The details about the functionalities of the registers can be found in [Gen08].

3.2.2 Host operating system

A backend, or a device driver, is a type of program that allows high-level computer programs to interact with a hardware device with the aid of API. In most cases, those drivers will group several closely related hardware operation into a "routine" to facilitate the programming efficiency and make them accessible through the API as an "entry point".

However, the problem with SANE API is that it is initially developed to cater to the need of document scanning. Therefore, the API only provides the most common functionalities, such as start scanning, read data, and etc., though the hardware of the scanner is much more powerful. For example, the scanner chip

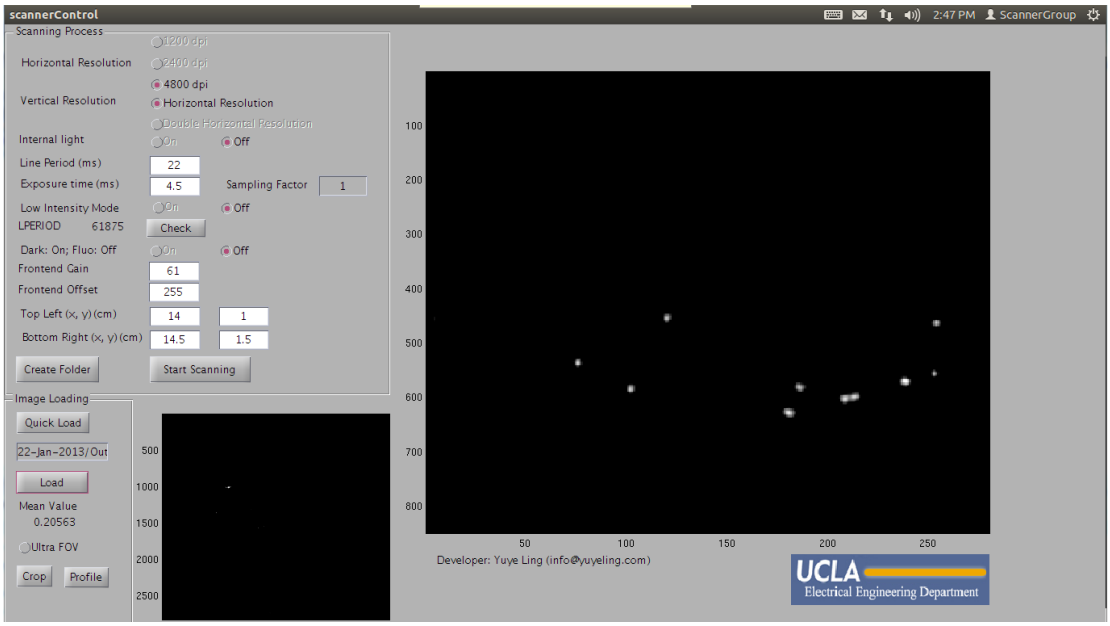

Figure 3.3: Graphic User Interface (GUI) for the scanner control

itself is capable of controlling sensor exposure, motor movement and etc., but none of those is supported by the SANE API.

Therefore, our approach is to implement more entry points in the SANE API and routines in SANE backend to meet our requirements. Since the SANE backend has already implemented a number of basic operations such as setting registers and reading registers, we can easily manipulate the values of the registers by using these existing routines.

3.3 The implementation of the control program

3.3.1 Existing functions provided by SANE API

As described in the manual for SANE API [SAN06], developers can build customized frontend programs by using the SANE library and the SANE functions. There are 10 functions that are most frequently used as listed below.

3.3.1.1 `sane_init` and `sane_exit`

`sane_init` function initializes the SANE environment and it must be called before calling any other SANE functions. After the initialization is finished, a value equals to `SANE_STATUS_GOOD` will be returned.

On the other hand, `sane_exit` function closes all the backend handles and shut down the SANE environment. No SANE functions other than `sane_init` can be called after it.

3.3.1.2 `sane_get_devices`, `sane_open` and `sane_close`

`sane_get_devices` is usually used to automatically detect the connected devices and to return the USB addresses of all available devices. `sane_open` can be called to assign handles for every devices. But at the end of each scanner session, all the handles should be given up by using `sane_close` to prevent memory leakage.

3.3.1.3 `sane_get_option_descriptor`, `sane_control_option` and `sane_get_parameters`

By calling SANE member function `sane_get_option_descriptor`, we can get the access to the list of option descriptors, which provide us with the information of the controllable parameters supported by the backend, such as scan resolution, the geometry of the scanning area (by designating the x, y coordinate of the top-left corner of the rectangular and that of its bottom-right counterpart), bit depth of the recorded image, shading table, and gamma table. Then by calling `sane_control_option()`, we can set the parameters mentioned above one by one. In reality, those set parameters will be sent to the aforementioned "routines" inside the backend. And those "routines" will process the parameters and manipulate the registers' value accordingly.

For example, as to the SANE backend for GL847 chipsets, the scan resolution

is listed 6^{th} among all the control parameters. Therefore, we can set the resolution of the scan to a value up to 4800 dpi we want by calling

```
scan_control_option (deviceHandle, 6, 1, intValue, &info);
```

where `deviceHandle` is the handle created for the current scanner, `6` represents the ranking number of the control parameter that we desire to manipulate, `1` is the value that we want to set for the control parameter, while the `intValue` is the value we want to set and the `info` gives the return information of the operation. Then, based on the implementation of the "routine", the set value will be written into the corresponding registers.

Finally, `sane_control_option` can be used to check the current value of any parameters that are defined by the backend.

3.3.1.4 `sane_start`, `sane_read` and `sane_close`

After setting all the parameters required by the user, we can now start the scanning process by calling function `sane_start`. Further using `sane_read` will enable retrieving image data from the device. Before exiting the program, we also need to call `sane_close` to end the scanning session.

The code flow for the SANE API can be illustrated by Figure 3.4

3.3.2 Newly introduced functions

In order to build a control program that can provide us all the functionalities we need and make the best use of the existing software structure, I tried to introduce more customized "routines" to the SANE API. This was done by modifying the `genesys.h` head file and `genesys.c` source file, since the routines are defined in `genesys.h` and implemented in `genesys.c`.

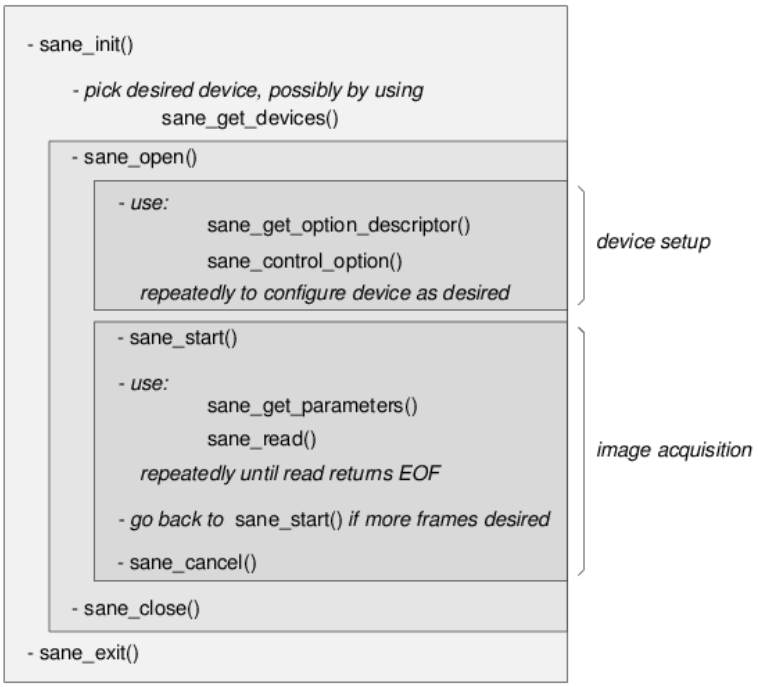

Figure 3.4: Code flow for the SANE API [SAN06]

I inserted the new control parameters into the enumerate group `Genesys_Options` in `genesys.h`. After that we need to further modify the `genesys.c` file and implement the routine by setting corresponding registers. Several low level functions such as `sane_genesys_read_register` and `sane_genesys_read_register` can be called to facilitate the process of manipulating the registers.

3.3.2.1 Line period

In the scanner system, the line period mandates the rotating speed of the stepper motor, and further the velocity of the scanner head. The unit of this parameter is system clock, and the value is given by register `0x38` and `0x39`, which are corresponding to the high byte and low byte of the line period, respectively. Given that the system clock of the scanner is fixed (24MHz), I just convert the unit from clock to ms for simplicity in the GUI.

3.3.2.2 Exposure time

As I have mentioned before, the triple-LED illumination of the CIS scanner system is moving along with the scanner head. Meanwhile, the LEDs keep flashing different colors periodically in accordance with the exposure time set by the user. Therefore, though the scanner image sensors themselves are monochromatic, they can still retrieve color information of the sample. As a result, there is no option to directly set the exposure time of the pixel in GL847 chipset. On the other hand, the pixels' exposure time is indirectly controlled by tuning the "exposure time" of the LED illuminations.

However, the above descriptions are only applicable to the situation when internal illumination is adopted. In our case, if we are using external illumination, the pixels will remain turned on all the time. Thus, there is no need for us to set the "exposure time" for the LED, and the exposure time of the pixel will be automatically set to be one third of the line period.

3.3.2.3 Frontend gain, frontend offset

In GL847 chipset, there is an analog frontend (also known as analog-digital converter (A/DC)), which is responsible for converting the induced current to digital signal. Therefore, the meaning of those two parameters become quite obvious: one for providing a constant offset, while the other for boosting the sensitivity.

3.3.2.4 Other useful functionalities

In order to simplify the controlling procedure, a straightforward GUI is created in MATLAB. The user interface is presented in Figure 3.3. Also thanks to the mighty MATLAB, we find that most functions we need to analyze the image have already been integrated. For example, we can use `improfile` to get the profile of a given cross section in the image and `imzoom` to zoom in a certain area and check

the details as shown in Figure 3.3.

CHAPTER 4

Image correction and post processing

In order to get a decent image, we need to do extra image correction or post processing on the raw data.

4.1 Offset and gain correction settings for Analog-Digital Converter (ADC)

As an analog device, the CMOS image sensor array that we are using in the scanner has several inherent problems.

- Even when the CMOS image sensor are scanning a pure dark object, we will still be able to obtain nonzero values for pixels, which is due to the dark current. Therefore, I set the "offset" for ADC to bias them.
- Due to the distinct response curve for each pixel, a pure white object may result in saturation for some pixels. Thus, we need to set the "gain" for each channel to make sure all the pixel values should be falling within the range of the ADC.

Therefore, following algorithm can be used to roughly correct the offset and gain.

- **Step 1:** Set the gain to be 0, and offset to be 0. Scan a dark area with no illumination. Get the image, and average it in the main scanning direction. Then, set the "offset" to be the minimum value of the average.

- **Step 2:** Scan the dark image again, and get the image. Average it again in the main scanning direction, and save it as "offset table".

- **Step 3:** Scan a bright area with illumination. Get the image (in different channels) and average it in main scanning direction. Then calculate the maximum value for each channel of the image. Divide the maximum value of the ADC by the maximum value for each channel, and set them to be the "gain", respectively.

After following the above procedures, the ADC for the CMOS sensor array should have been correctly configured.

4.2 Shading table

In the previous section, we have discussed the effect of two parameters used in ADC. However, both parameters, i.e. "offset" and "gain" can only globally, roughly tune the dynamic range. More subtle pixel-level equalization should be performed by using shading table. Since the transfer curve of each pixel (and affiliated ADC) varies, we might get a non-uniform image even if we are imaging a reference white sheet with uniform illumination as shown in the following figure. In order to compensate this, a shading table can be set up to equalize it. The detailed steps are shown as follows,

- **Step 1:** Scan a bright area with uniform illumination, and scan a dark area without light. Get the two images and subtract one from the other. The difference shows the response of individual pixels to the same stimulus. Then, a coefficient can be calculated for each pixel.

- **Step 2:** Scan the sample, subtract the dark current from the resultant raw data and multiply the results by the coefficient. Then, we should get a corrected image.

Here we provide an example on how to equalize the entire FOV under fluorescent illumination.

Then, a comparison is made between a cropped part of the raw image and its post-proposed counterpart . And the comparison is illustrated in Figure 4.2

4.3 Deconvolve the motor movement effect

4.3.1 Motivation

For the scanner system, one of the most essential parts is the motor. Considering that we are using a one-dimensional sensor array that extends in x direction (sub-scanning direction), we need to slowly move the sensor array in the y direction (main-scanning direction) in order to get the image over the entire surface. Therefore, we require the motor to move accurately and steadily to form a uniform grid in the y direction. In the meantime, the sensor array itself is continuously capturing images. In the ideal case, the scanner should capture one frame, which corresponds to one line of the whole image, once the motor moves one step. In this way, we will be able to get an image that looks identical to that achieved by a two-dimensional image sensor. And the width of the one-dimensional sensor array's pixel (in x direction) will correspond to that of two-dimensional grid's, while the step size of the movement will correspond to the height of two-dimensional grid. And that's how the default scanner driver works.

In x direction, the physical size of the pixel is fixed and invariant with the movement. However, in y direction, the resolution is related to the step size. So, it seems to be a very natural thought that we can increase the resolution by reducing the step size. And if we reduce the step size to be smaller than the size of the pixel, the resultant image will be equivalent to the results from using "shift and add" algorithm [FRE04].

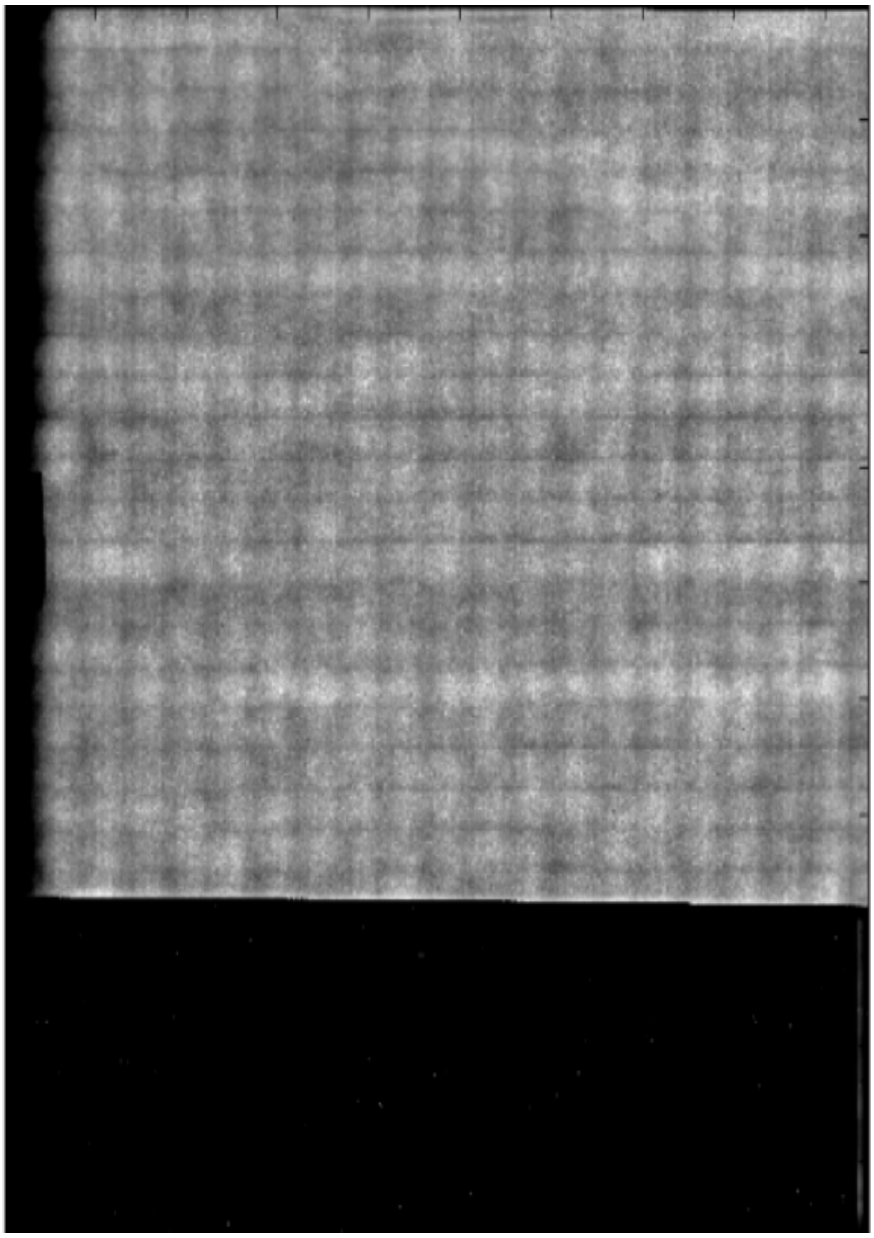

Figure 4.1: Raw image of a letter paper. Size of the paper within field-of-view (10 cm by 10 cm) @ 1200 dpi (exposure time = 15 ms).

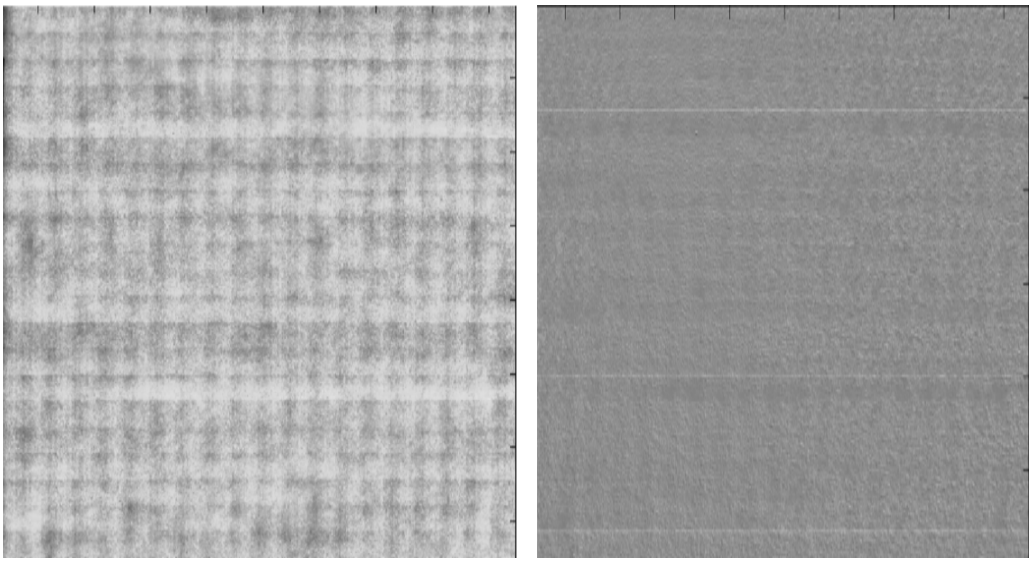

(a) (b)

Figure 4.2: White copy paper(a) raw image; (b) after applying shading operation. Field of view (10 cm by 10 cm) @ 1200 dpi

However, the step size has its lower limit, which is defined by the resolution of motor. In our case, the smallest step size is 1/8 step. Upon reaching this limit, we can no longer reduce it.

Fortunately, we have another parameter, which is the sampling rate (has the same unit as the frequency) of the sensor. In general cases, the exposure time, whose reciprocal is the sampling rate, of the sensor is synchronized with the line period, which is the time used to move one step (or line), of the motor. By reducing the exposure time, we can acquire subpixel information of the sample. In other words, if we can raise the sampling rate of the sample, more frames will be sequentially taken, while the motor is moving only one step. Therefore, there might be a chance that the several points situate between the two adjacent steps will be sampled, and the information of those sub-pixel points will be preserved.

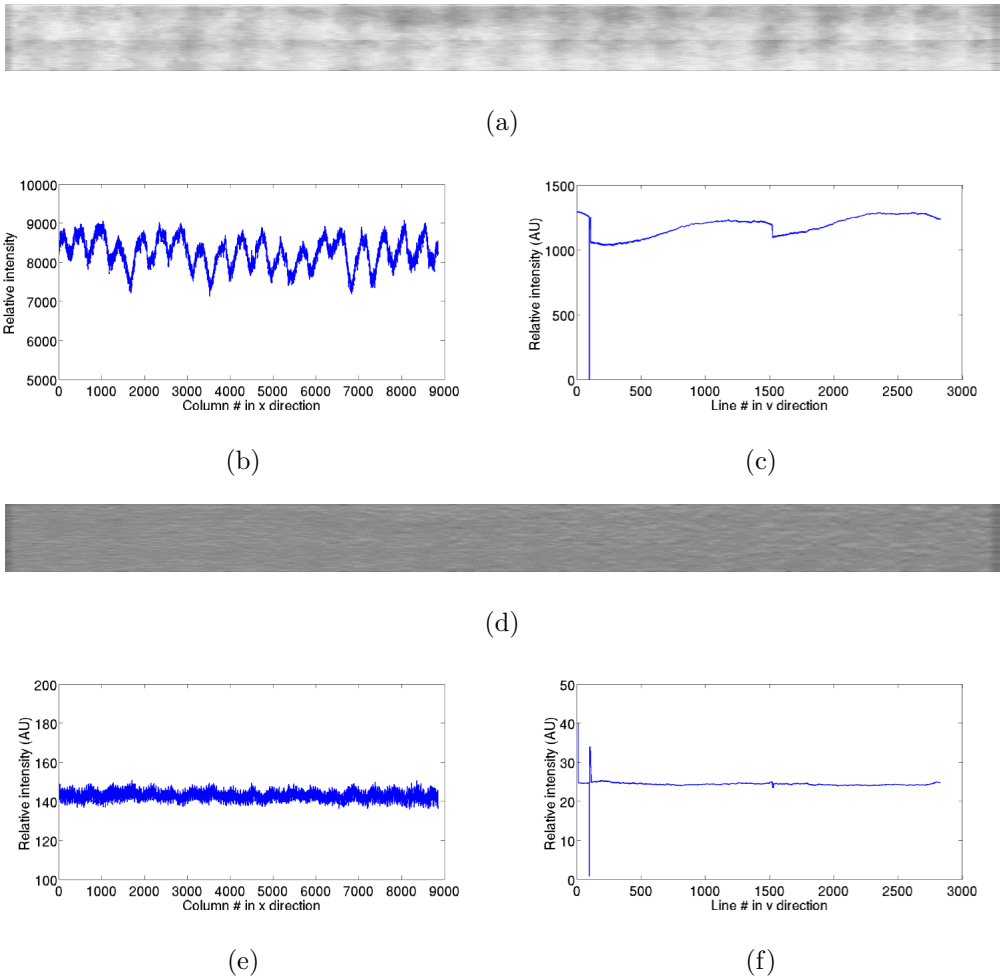

Figure 4.3: (a) raw image (b) x profile (c) y profile of the fluorescent illumination. (d) equalized image (e) x profile (f) y profile of the fluorescent illumination.

4.3.2 Mathematical model

Mathematically, the new system that has the capability of sub-pixel sampling can be represented by the following equation,

$$I(m,n) = I(x, y(t)) \sum_{-\infty}^{\infty} \delta(x - mT_x, y(t - nT_t)) \tag{4.1}$$

where $I(m,n)$ is a discrete function, while $I(x, y(t))$ is its continuous counterpart. $\sum_{-\infty}^{\infty} \delta(x - mT_x, y(t - nT_t))$ is the 2D sampling function. T_x determines the sampling period in x direction and T_t determines that in t axis.

As you might have noticed, $y(t)$ appears in Equation 4.1 instead of y, which makes the resultant image I is a function of time in y direction. It is because we are now attempting to unveil the information hidden in the sub-pixel domain. In that domain, we can no longer neglect the characteristics of the motor movement, which is nonlinearly dependent on the time.

Originally, our motivation is to increase the sampling rate in y direction to restore the object more precisely. However, when we reach the sub-pixel domain, we can no longer treat each step as an elementary unit and we have no idea how the motor behaves during each step. Though the sampled frames (or lines) is equally spaced in time domain, it might not be the case for space domain. This idea should work perfectly, if and only if the sensor array is making a uniform rectilinear motion throughout the whole process. In this case, the position of the sensor array in y direction is linearly dependent on the time lapsed,

$$y = vt \tag{4.2}$$

where v gives the velocity of the movement. Then, we can easily plug this equation into the previous one and apply typical shift and add algorithm.

Unfortunately, it is not the case. As we can see from Figure 4.4, the stepper motor is actually moving with nonlinearly dependency on time within a step.

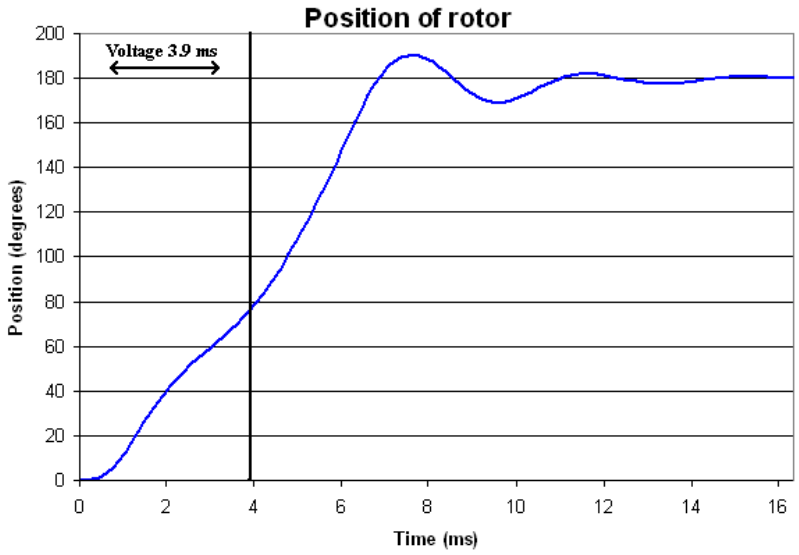

Figure 4.4: The rotation curve of stepper motor.
(http://www.infolytica.com/en/applications/ex0101/)

4.3.3 Challenge

Now, here comes the challenge.

Can we use some kind of technique to acquire the curve that characterize the movement of the motor based on the information we get?

Since if we can get this curve correctly, then we might be able to restore the image and convert it from (x, t) space to (x, y) space. After that, we can further apply the super-resolution algorithm upon the image, which could fundamentally improve the resolution of our system.

4.3.4 Clue

Actually, as we can see from the Figure 4.5, the air force target is placed with a tilting angle and we have severe artifacts in the vertical neighborhood of the edge. Ideally, due to the pixel size, the edge we get should look like saw teeth, and

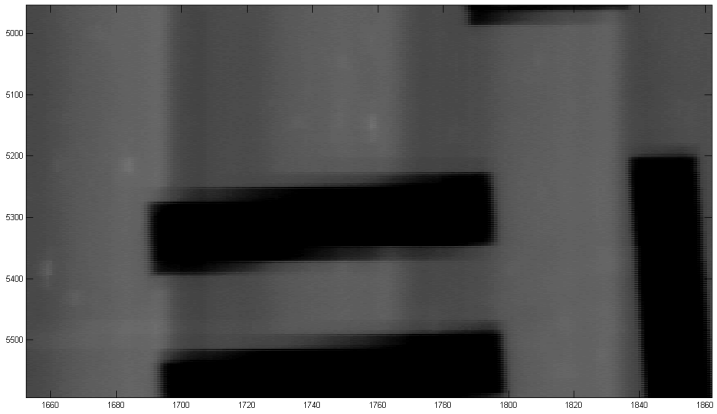

Figure 4.5: Raw image of a tilted US air force target. We can find that the horizontal edge of the bar looks different from its vertical counterpart

its envelope should be corresponding to the titling angle. However, in this case, what we see are several large blurred rectangles and within those rectangles the edge looks discontinuous. If we further look into the cross section, we can see the jumps and the following oscillations, while for a normal optical system, the edge should be smooth and Gaussian-like. Moreover, the period of the jump actually corresponds to one full step. I suspect, those are actually due to the nonlinear motor movement with one step as shown in the previous figure.

Currently, we are still progressing on this issue.

4.4 Gigapixel image rendering

Due to the huge size of the raw data (Over 2.15 gigapixels for full field of view @ 4800 dpi), it is not possible for us to render them in a single shot. Most mainstream computer does not have such a large memory to either process or load the image.

However, by using the HDView, which developed by Microsoft, we can easily

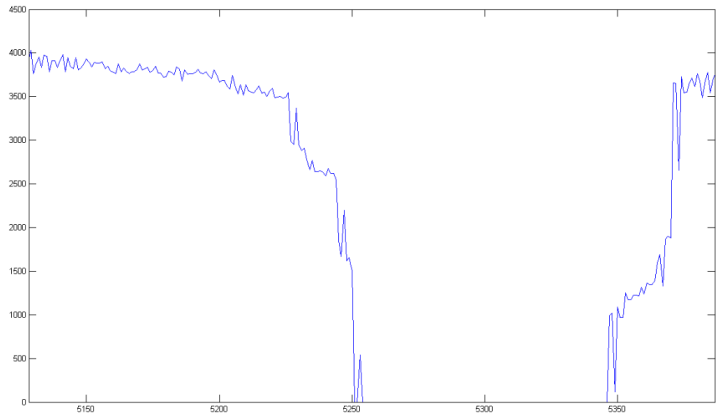

Figure 4.6: The cross-section view of the previous image

achieve our goals. The generated gigapixel image will be attached as a complimentary document.

CHAPTER 5

Experiments and results

To validate the proposed system, we designed several experiments in both dark-field mode and fluorescence mode. For dark-field setups, microspheres as small as 4 μm can be detected, while in fluorescence mode signals from 10 μm microspheres can be picked up.

5.1 Sample preparation

In this experiment, three samples are prepared.

- Sample 1: 10 μm fluorescence beads and 10 μm non-fluorescence beads.
- Sample 2: 10 μm fluorescence beads and 4 μm fluorescence beads.
- Sample 3: 10 μm fluorescence beads and 5 μm non-fluorescence beads.

We first diluted those microspheres (Duke standards, NIST traceable polymer microspheres, 10 μm and 5 μm.) 1:1000 from the solution into deionized water. Then, we mixed those solution according to the requirement of the sample. After that, we deposited the resultant solution on the top of the mylar polyster sheet (7 cm by 7 cm), which had been cleaned and surface treated with high frequency generator beforehand.

5.2 Scanner imaging and results

Microscope observation was made before we place the sample onto the scanner. However, due to the huge mismatch of the FOV between conventional optical microscope and scanner, it is impossible for us to provide a full FOV microscopic comparison as large as 600 cm^2. Alternatively, we only drew a small circle on the sample, and imaged that area under the microscope.

After that, a scanner examination was performed over the entire FOV ($\sim$20 cm by 30 cm). The optical resolution of the linear CMOS sensor array was set to be 4800 dpi ($\sim$5.29 μm).

A downsampled version of the resultant gigantic image is provided below, while a zoomable version of the raw image is hosted online. Moreover, images of several smaller area within the original dark-field result are compared with its microscopic counterpart.

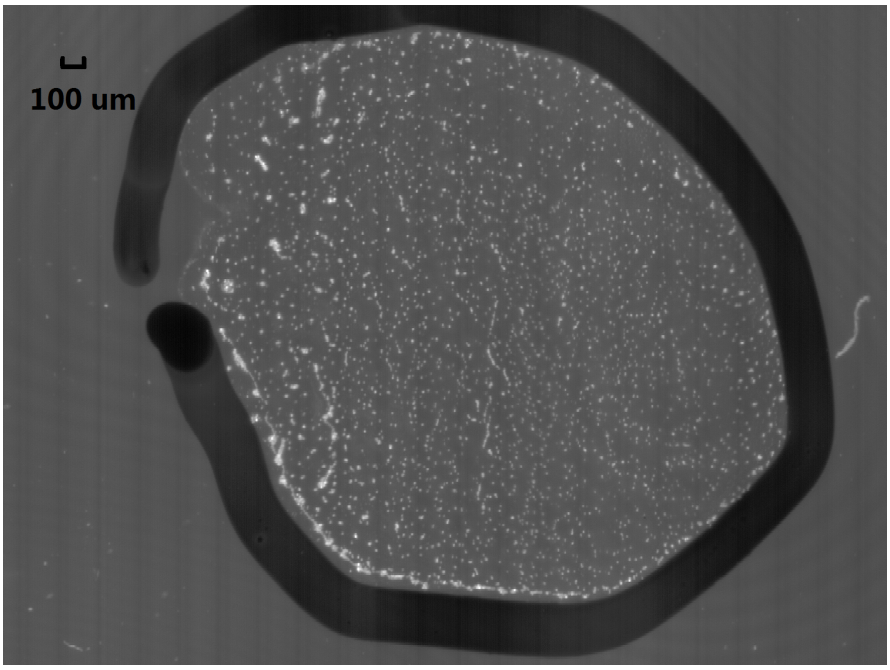

(a)

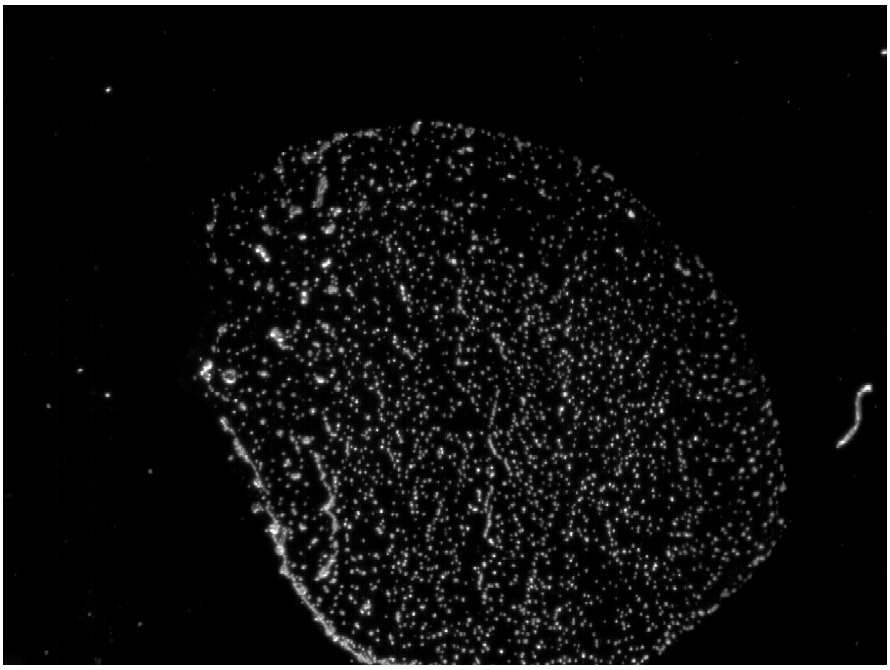

(b)

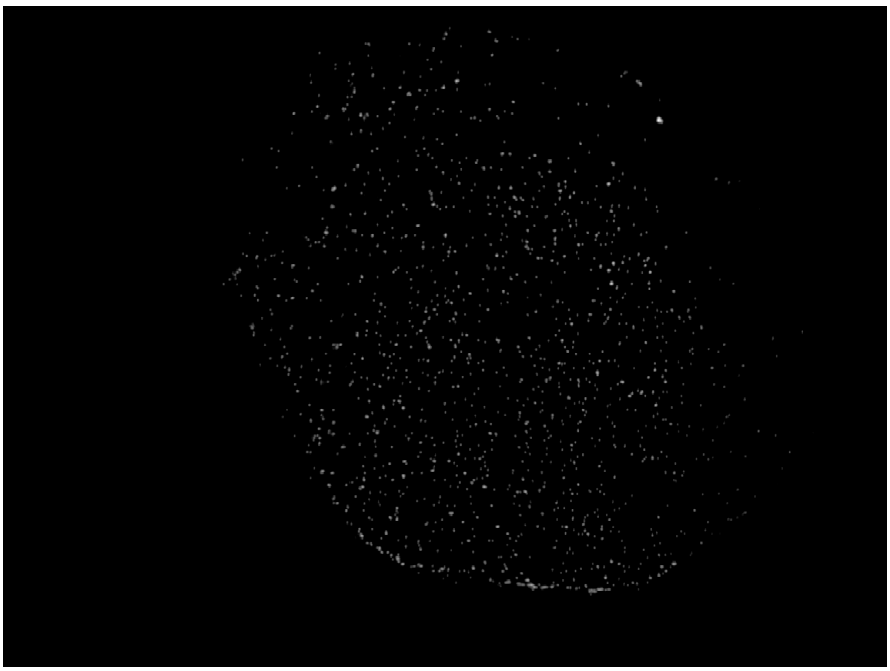

(c)

Figure 5.1: Scanned image of Sample 1 (10 μm fluorescence beads and 10 μm non-fluorescence beads). (a) Bright field (ambient light) (b) Dark field (c) Fluorescence

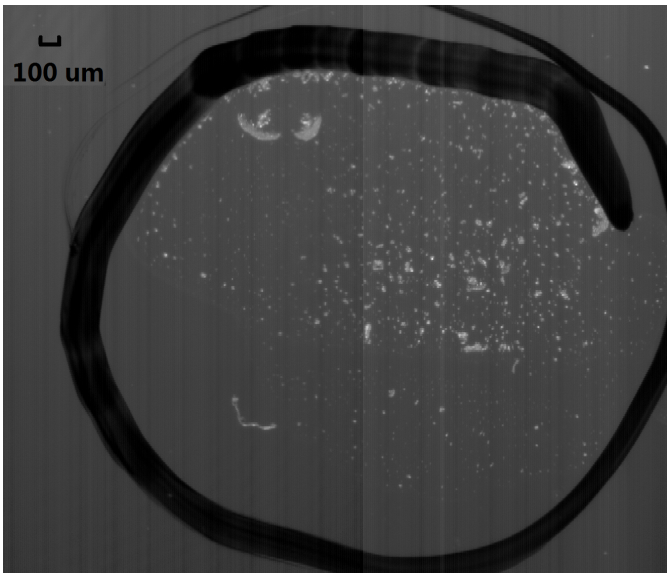

(a)

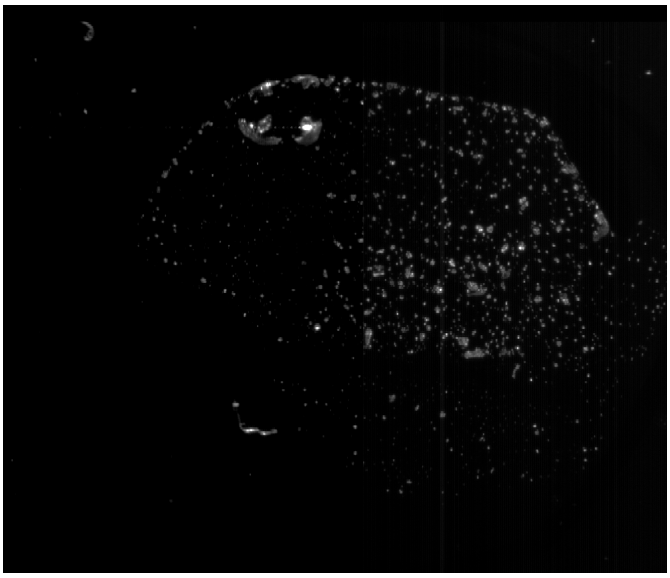

(b)

Figure 5.2: Scanned image of Sample 2 (10 μm fluorescence beads and 4 μm fluorescence beads). (a) Bright field (ambient light) (b) Dark field

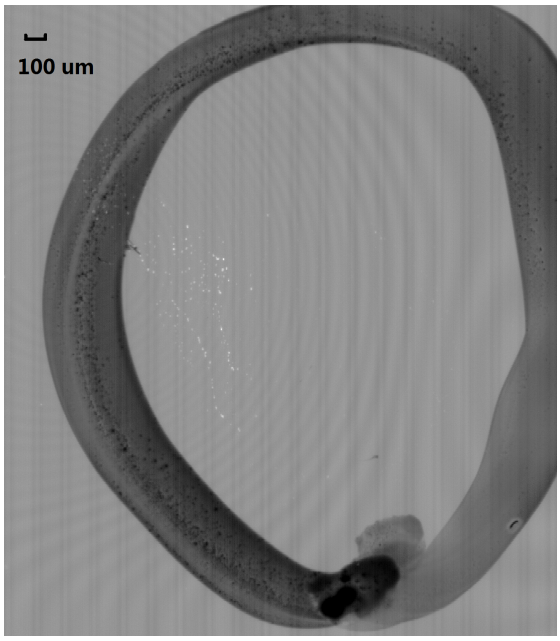

(a)

(b)

Figure 5.3: Scanned image of Sample 3 (10 μm fluorescence beads and 5 μm non-fluorescence beads). (a) Bright field (ambient light) (b) Fluorescence

References

[AAC12] Serap Altay Arpali, Caglar Arpali, Ahmet F. Coskun, Hsin-Hao Chiang, and Aydogan Ozcan. "High-throughput screening of large volumes of whole blood using structured illumination and fluorescent on-chip imaging." *Lab Chip*, **12**:4968–4971, 2012.

[Bak56] Hnery Baker. "Drawing of microscopes owned by Antonie van Leeuwenhoek.", 1756.

[Bar88] J.J. Barton. "Photoelectron holography." *Physical review letters*, **61**(12):1356–1359, 1988.

[Ben69] S. A. Benton. "Hologram reconstructions with extended incoherent sources." *J. Opt. Soc. Am*, **59**:1545C1546, 1969.

[CFD06] N.S. Claxton, T.J. Fellers, and M.W. Davidson. "Laser scanning confocal microscopy." *Olympus. Available online at http://www. olympusconfocal. com/theory/LSCMIntro. pdf*, 2006.

[CK50] A.H. Coons and M.H. Kaplan. "Localization of antigen in tissue cells II. Improvements in a method for the detection of antigen by means of fluorescent antibody." *The Journal of experimental medicine*, **91**(1):1–13, 1950.

[CSO10] Ahmet F. Coskun, Ting-Wei Su, and Aydogan Ozcan. "Wide field-of-view lens-free fluorescent imaging on a chip." *Lab Chip*, **10**:824–827, 2010.

[CSS11] Ahmet F. Coskun, Ikbal Sencan, Ting-Wei Su, and Aydogan Ozcan. "Lensfree Fluorescent On-Chip Imaging of Transgenic ¡italic¿Caenorhabditis elegans¡/italic¿ Over an Ultra-Wide Field-of-View." *PLoS ONE*, **6**(1):e15955, 01 2011.

[CTE94] M Chalfie, Y Tu, G Euskirchen, WW Ward, and DC Prasher. "Green fluorescent protein as a marker for gene expression." *Science*, **263**(5148):802–805, 1994.

[Den62] Y.N. Denisyuk. "On the reflection of optical properties of an object in a wave field of light scattered by it." *Doklady Akademii Nauk SSSR*, **144**(6):1275, 1962.

[FEM11] S.C. Fox, C. Eliopoulos, I. Moutafi, and S.K. Manolis. "A Simple Technique for Imaging the Human Skeleton Using a Flatbed Scanner*." *Journal of Forensic Sciences*, **56**:S154–S157, 2011.

[FRE04] S. Farsiu, M.D. Robinson, M. Elad, and P. Milanfar. "Fast and robust multiframe super resolution." *Image Processing, IEEE Transactions on*, **13**(10):1327 –1344, oct. 2004.

[Gab48] D. Gabor. "The invention of holography." *Nature*, **161**:777–778, 1948.

[Gab49] D. Gabor. "Microscopy by Reconstructed Wave-Fronts." *Proceedings of the Royal Society of London. Series A, Mathematical and Physical Sciences*, **197**(1051):454–487, Jul 1949.

[Gen08] Genesys Logic. *Datasheet: GL846 High Speed USB 2.0 2-in-1 Scanner Controller With Fast ADF*, 1.05 edition, January 2008.

[GL67] J. W. Goodman and R. W. Lawrence. "DIGITAL IMAGE FORMATION FROM ELECTRONICALLY DETECTED HOLOGRAMS." *Applied Physics Letters*, **11**(3):77–79, 1967.

[GoF12] GoFoton. "SELFOC Lens Array (SLA) - Technical Charts.", Nov 2012.

[GXJ06] J. Garcia-Sucerquia, W. Xu, S.K. Jericho, P. Klages, M.H. Jericho, and H.J. Kreuzer. "Digital in-line holographic microscopy." *Applied optics*, **45**(5):836–850, 2006.

[Hoo67] Robert Hooke. *Micrographia: or some physiological descriptions of minute bodies made by magnifying glasses : with observations and inquiries thereupon.* Printed for John Martyn, printer to the Royal Society, and are to be sold at his shop at the Bell a little without Temple Barr, 1667.

[ISM10] Serhan O. Isikman, Ikbal Sencan, Onur Mudanyali, Waheb Bishara, Cetin Oztoprak, and Aydogan Ozcan. "Color and monochrome lensless on-chip imaging of Caenorhabditis elegans over a wide field-of-view." *Lab Chip*, **10**:1109–1112, 2010.

[KO80] Motoaki Kawazu and Yukio Ogura. "Application of gradient-index fiber arrays to copying machines." *Appl. Opt.*, **19**(7):1105–1112, Apr 1980.

[Kre02] H.J. Kreuzer. "Holographic microscope and method of hologram reconstruction.", June 25 2002. US Patent 6,411,406.

[Kre09] Frederik C. Krebs. "Fabrication and processing of polymer solar cells: A review of printing and coating techniques." *Solar Energy Materials and Solar Cells*, **93**(4):394 – 412, 2009. ¡ce:title¿Processing and Preparation of Polymer and Organic Solar Cells¡/ce:title¿.

[KRK09] M. Kanka, R. Riesenberg, and HJ Kreuzer. "Reconstruction of high-resolution holographic microscopic images." *Optics letters*, **34**(8):1162–1164, 2009.

[KSO02] Jan Krger, Kirat Singh, Alan O'Neill, Carl Jackson, Alan Morrison, and Peter O'Brien. "Development of a microfluidic device for fluorescence activated cell sorting." *Journal of Micromechanics and Microengineering*, **12**(4):486, 2002.

[Lac99] Alan J. Lacey. *Light Microscopy in Biology: A Practical Approach.* Oxford University Press, 1999.

[LU62] Emmett N. Leith and Juris Upatnieks. "Reconstructed Wavefronts and Communication Theory." *J. Opt. Soc. Am.*, **52**(10):1123–1128, Oct 1962.

[MD12] D.B. Murphy and M.W. Davidson. *Fundamentals of light microscopy and electronic imaging.* Wiley-Blackwell, 2012.

[MML13] Onur Mudanyali, Euan McLeod, Wei Luo, Alon Greenbaum, Ahmet F Coskun, Yves Hennequin, Cédric P Allier, and Aydogan Ozcan. "Wide-field optical detection of nanoparticles using on-chip microscopy and self-assembled nanolenses." *Nature Photonics*, 2013.

[Nob08] "The Nobel Prize in Chemistry 2008.", 10 2008.

[OD08] Aydogan Ozcan and Utkan Demirci. "Ultra wide-field lens-free monitoring of cells on-chip." *Lab Chip*, **8**:98–106, 2008.

[Paw95] J. B. Pawley. *Handbook of Biological Confocal Microscopy, 2nd. ed.* Plenum, 1995.

[PEW92] Douglas C. Prasher, Virginia K. Eckenrode, William W. Ward, Frank G. Prendergast, and Milton J. Cormier. "Primary structure of the Aequorea victoria green-fluorescent protein." *Gene*, **111**(2):229 – 233, 1992.

[Rod] "Wire-wound metering rod coating technology." Online.

[RRA09] Charles Richard, Alan Renaudin, Vincent Aimez, and Paul G Charette. "An integrated hybrid interference and absorption filter for fluorescence detection in lab-on-a-chip devices." *Lab Chip*, **9**(10):1371–1376, 2009.

[Rus81] P.St.J. Russell. "Optical volume holography." *Physics Reports*, **71**(4):209 – 312, 1981.

[SAN06] SANE (Scanner Access Now Easy). *SANE Standard*, 1.05 edition, April 2006.

[Shi79] O. Shimomura. "Structure of the chromophore of Aequorea green fluorescent protein." *FEBS Letters*, **104**(2):220 – 222, 1979.

[Shi05] O. Shimomura. "The discovery of aequorin and green fluorescent protein." *Journal of Microscopy*, **217**(1):3–15, 2005.

[SJ94] U. Schnars and W. Jüptner. "Direct recording of holograms by a CCD target and numerical reconstruction." *Appl. Opt.*, **33**(2):179–181, Jan 1994.

[SKQ12] Kate Sullivan, Johannes Kloess, Chen Qian, Donald Bell, Alan Hay, Yi Pu Lin, and Yan Gu. "High throughput virus plaque quantitation using a flatbed scanner." *Journal of Virological Methods*, **179**(1):81 – 89, 2012.

[SST09] Sungkyu Seo, Ting-Wei Su, Derek K. Tseng, Anthony Erlinger, and Aydogan Ozcan. "Lensfree holographic imaging for on-chip cytometry and diagnostics." *Lab Chip*, **9**:777–787, 2009.

[TAO12] TAOS. "Intelligent opto sensor designer's notebook.", Nov 2012.

[VAV06] C. Vonesch, F. Aguet, J.-L. Vonesch, and M. Unser. "The Colored Revolution of Bioimaging." *IEEE Signal Processing Magazine*, **23**(3):20–31, May 2006.

[YHC09] C.H. Yeh, C.Y. Hung, T.C. Chang, H.P. Lin, and Y.C. Lin. "An immunoassay using antibody-gold nanoparticle conjugate, silver enhancement and flatbed scanner." *Microfluidics and nanofluidics*, **6**(1):85–91, 2009.

[ZOY12] G. Zheng, X. Ou, and C. Yang. "Gigapixel microscopy using a flatbed scanner." *arXiv preprint arXiv:1209.4045*, 2012.